The Cryosphere, 20, 5041–5060, 2026
https://doi.org/10.5194/tc-20-5041-2026

The Cryosphere
Open Access

Enabling ice sheet models to capture centennial-scale solid Earth feedback with relative ease and sufficient accuracy

Surendra Adhikari[1], **Lambert Caron**[1], **Erik R. Ivins**[1], **Holly K. Han**[1], **Luc Houriez**[1,2], **and Eric Larour**[1]

[1]Jet Propulsion Laboratory, California Institute of Technology, Pasadena, CA 91011, USA
[2]Department of Mechanical Engineering, Stanford University, Stanford, CA 94305, USA

Correspondence: Surendra Adhikari (surendra.adhikari@jpl.nasa.gov)

Received: 23 July 2025 – Discussion started: 4 October 2025
Revised: 4 June 2026 – Accepted: 14 August 2026 – Published: 8 September 2026

Abstract. There is a growing consensus on the critical role that solid Earth processes play in influencing marine ice sheet dynamics over centennial timescales. A large body of literature shows that the feedback mechanisms associated with the solid Earth's gravitational, rotational, and deformational (GRD) response to ice mass loss slow the progression of ice sheet instabilities. However, due to the limited availability of efficient coupled system models, the specific characteristics of the feedback mechanisms, their sensitivities to ice sheet processes, and their impacts on centennial-scale sea level projections remain largely unexplored. This paper introduces a simple method that enables ice sheet models to address this limitation by capturing GRD effects with relative ease and sufficient accuracy. The proposed method uses precomputed Green's functions for a suite of radially symmetric Earth models and convolves them with mass changes within the ice sheet model. This approach straightforwardly retrieves the induced geoid and bedrock topography fields, paving the way for efficient coupling between ice sheet dynamics and leading-order solid Earth response on decadal to centennial timescales.

1 Introduction

An improved understanding of ice sheet dynamics is essential for producing accurate global and regional sea level projections. To achieve this, sophisticated ice sheet models that capture higher-order processes and feedback mechanisms are necessary. The ice sheet modeling community has increasingly recognized the importance of dynamic interactions between ice sheets and solid Earth processes over decadal and longer timescales. As ice mass changes, it exerts spatiotemporal variations in pressure on the solid Earth surface, changing bedrock topography and the geoid field, and thus sea level. These alterations in topography and sea level significantly influence marine ice sheet dynamics. They do so by affecting the retrograde bed slope, reinforcing pinning points and bedrock ridges, altering ocean heat transport patterns due to the modified shape of sub-shelf cavities, and influencing gravitational driving stress and surface mass balance through surface elevation and slope changes (e.g., Gomez et al., 2012; Adhikari et al., 2014; Larour et al., 2019; Albrecht et al., 2024; Kreuzer et al., 2025).

Several established methods of varying complexity exist for capturing solid Earth feedback in ice sheet models. The most straightforward approach relies on the two-layer framework of Lingle and Clark (1985), consisting of an elastic lithosphere overlying a viscously relaxing mantle half-space (e.g., Ivins and James, 1999; Adhikari et al., 2014; Swierczek-Jereczek et al., 2024). Building on this, Meur and Huybrechts (1996) introduced a formulation in which the lithosphere overlies a finite-thickness asthenosphere layer, commonly referred to as the Elastic Lithosphere Relaxing Asthenosphere (ELRA) model. A more complex method involves modeling a self-gravitating, density-stratified, viscoelastic Earth with a radially symmetric structure that typically includes an elastic lithosphere, a multi-layered Maxwellian mantle, and an inviscid core (e.g., Peltier, 1974; Farrell and Clark, 1976). Generally used in glacial isostatic adjustment (GIA) studies, this class of models enables capturing the full gravitational, rotational, and deformational

(GRD) feedback to ice sheet dynamics (e.g., Gomez et al., 2012; Konrad et al., 2015; Larour et al., 2019; Han et al., 2022). More comprehensive approaches, such as those involving three-dimensional Earth structure (e.g., Albrecht et al., 2024; Gomez et al., 2024) and sophisticated non-Maxwellian mantle rheology (Houriez et al., 2025; Coonin et al., 2026), are currently being explored to enhance our understanding of feedback mechanisms.

All these models come with caveats, especially regarding their suitability for high-resolution coupled simulations. Downsides may range from being too simplistic (e.g., half-space models) to involving complex numerical implementations that demand significant computational cost (e.g., global GIA models). As a result, many ice sheet models, including those involved in the Ice Sheet Model Intercomparison Project (ISMIP), often omit GRD feedback. Among the 16 models that contributed to the ISMIP Antarctic Ice Sheet projections extending to 2300 (Seroussi et al., 2024), only four include any representation of solid Earth feedback, and even these primarily rely on the most simplified ELRA approach. The omission of GRD feedback, or its representation through the ELRA approximation, may bias projections of grounding line retreat and sea level change (e.g., Konrad et al., 2016; Larour et al., 2019). GIA emulators (Lin et al., 2023; Love et al., 2024) and more realistic regional models (Coulon et al., 2021; Swierczek-Jereczek et al., 2024; van Calcar et al., 2026) are emerging as promising options that offer reduced computational cost. Further investigation is needed into both traditional geophysical modeling approaches and emerging machine learning techniques to improve model efficiency and accuracy and simplify the coupling strategy.

Here we present a simple method that enables ice sheet models to capture solid Earth feedback requiring neither additional model development nor computational cost. A primary motivation for this research is to enhance ISMIP's current and future undertakings by enabling greater participation in coupled ice/Earth simulations, with direct implications for future Intergovernmental Panel on Climate Change (IPCC) reports that cater to planners and policymakers. We therefore focus on capturing the leading-order feedback signals over centennial timescales for radially symmetric Earth structures. We show that the direct effects of ice mass change account for over 90 % of the self-consistent GRD feedback signals in a radially symmetric Earth. In order to capture this leading process, it suffices to convolve the evolving mass change with time-variable Green's functions that characterize the solid Earth response to unit surface loads. By leveraging an extensive library of precomputed Green's functions available for a suite of Maxwellian Earth structures (Adhikari and Caron, 2024), our proposed method facilitates the swift retrieval of the evolving geoid and bedrock topography fields as ice sheet models march forward in time, thus enabling straightforward coupling between the ice sheet and the solid Earth. An efficient coupling enhances our understanding of feedback mechanisms, facilitates sensitivity analysis, and strengthens uncertainty quantification through large ensemble simulation. Ultimately, these improvements will enable more reliable projections of ice sheet contribution to sea level change.

The proposed method differs fundamentally from the commonly used ELRA framework. Rather than approximating Earth response through lithospheric flexural rigidity and asthenospheric relaxation timescales, the Green's functions employed here are derived from solutions of the governing equations of mass conservation, linear momentum conservation, and self-gravitation for a full-depth multilayered viscoelastic Earth (Caron et al., 2026). This provides a more realistic representation of load-induced deformation and gravitational signals, consistent with the framework adopted in modern GIA modeling. Moreover, standard ELRA implementations typically neglect geoid change and associated gravitational feedbacks, focusing solely on bedrock adjustment. As will be demonstrated below, geoid variations can be significant and are largely governed by ice mass changes. Accounting for these effects is therefore essential in coupled ice/Earth simulations.

Like any simplified/regional method, ours comes with limitations. It does not satisfy self-consistency in GRD processes (Farrell and Clark, 1976; Milne and Mitrovica, 1998), nor does it conserve mass in the global domain of ice and ocean. The effects of rotational feedback (Milne and Mitrovica, 1998), farfield ice melting (Gomez et al., 2020), and coastline migration (Kendall et al., 2005) are ignored. Although we show that these processes play a secondary role on the timescale of interest, they are critical in longer-timescale simulations (e.g., glacial cycles) and they can only be accounted for by recursively solving the self-consistent sea level equation (e.g., Spada and Melini, 2019). Our method does not capture the effects of three-dimensional Earth structures (Gomez et al., 2020), although the appropriate choice of a regionally averaged one-dimensional structure may partially mitigate this deficiency (Albrecht et al., 2024; Han et al., 2025; van Calcar et al., 2026). We caution readers of these caveats for the appropriate use of our method, whose main purpose is to capture solid Earth feedback in centennial-scale simulations of modern or paleo ice sheets.

2 Proposed method

Assuming that atmospheric pressure variability does not induce meaningful solid Earth deformation on decadal and longer timescales, the surface loading problem in the present context only requires resolving the lateral mass transport between the ice sheet and the ocean. A conditional function describing the ice and ocean load on the solid Earth surface, termed the "loading function" L [$\mathrm{kg\,m^{-2}}$], at a given point in time t may be expressed as follows:

$$L(\boldsymbol{x},t) = \begin{cases} \rho_{\mathrm{i}} H(\boldsymbol{x},t) & \text{if } H(\boldsymbol{x},t) > F(\boldsymbol{x},t) \\ \rho_w R(\boldsymbol{x},t) & \text{otherwise.} \end{cases} \tag{1}$$

Here $\boldsymbol{x}$ is the 2-D position vector on the solid Earth surface, ρ_i is the ice density [$\mathrm{kg\,m^{-3}}$], ρ_w is the ocean density [$\mathrm{kg\,m^{-3}}$], H is the ice thickness [m], R is the relative sea level [m], and F is the flotation height for ice [m] (see Fig. 1).

Following Gregory et al. (2019), we define R as the mean sea level S [m] relative to the sea floor, both referenced to the same ellipsoid (typically WGS84). We assume the sea floor is same as the bedrock B [m]. Mathematically,

$$R(\boldsymbol{x},t) = S(\boldsymbol{x},t) - B(\boldsymbol{x},t). \tag{2}$$

In mean sea level S, "mean" refers to a time-mean over tides and high-frequency waves. This distinction is irrelevant in GRD modeling. However, we maintain the terminology to align with the literature.

The flotation height for ice F [m] follows the principle of hydrostatic equilibrium and is given by

$$F(\boldsymbol{x},t) = \frac{\rho_w}{\rho_\mathrm{i}} \max\left[R(\boldsymbol{x},t), 0\right]. \tag{3}$$

The condition in Eq. (1) implies that the solid Earth is loaded by the ice sheet in the grounded portion of the marine (and terrestrial) ice sheet and by the ocean otherwise (Fig. 1a).

Numerical modeling requires discretizing the continuous loading function into p computational grids (having q nodes) and m time intervals: $[t_0,t_1]$, $[t_1,t_2]$, …, $[t_{m-1},t_\mathrm{m}]$. Spatial grids and time intervals do not have to be uniformly discretized. We may now express Eq. (1), in the units of mass [kg] and with the new notation $\mathcal{L}$, in its discrete form as follows:

$$\begin{aligned}\mathcal{L}(\boldsymbol{x}',t) \quad &= \Bigg[\overline{L}(\boldsymbol{x}',t_0) + \sum_{i=1}^{m}\left\{\overline{L}(\boldsymbol{x}',t_\mathrm{i}) - \overline{L}(\boldsymbol{x}',t_{i-1})\right\} \\ &\quad \mathcal{H}(t-t_\mathrm{i})\Bigg]A(\boldsymbol{x}'), \\ &= \mathcal{L}(\boldsymbol{x}',t_0) + \sum_{i=1}^{m} \Delta\mathcal{L}(\boldsymbol{x}',t_\mathrm{i})\ \mathcal{H}(t-t_\mathrm{i}),\end{aligned} \tag{4}$$

Here $\boldsymbol{x}'$ is the position of the center of the grid-cell or element, A is the elemental area [$\mathrm{m^2}$], and $\overline{L}$ [$\mathrm{kg\,m^{-2}}$] is the spatial mean of L over that area. As shown in Fig. 1b, we recommend placing the surface load at the grid centers, $\boldsymbol{x}'$, instead of at the nodes or vertices, $\boldsymbol{x}$, where we assess the solid Earth response. This is important because the Green's functions we intend to use contain inherent singularities at the loading point (Longman, 1962). In the equation, $\mathcal{H}$ is the Heaviside step function that takes the value of unity for $t \geq t_\mathrm{i}$ and zero otherwise. It ensures that we impose the stepwise load change on the solid Earth surface at the end of each time interval (Fig. 1c). For the period $-\infty < t < t_1$, the surface load is held constant to its initial or reference value $\mathcal{L}(\boldsymbol{x}',t_0)$, and we assume that the solid Earth is in hydrostatic equilibrium. As such, only the change in load induces solid Earth response, which can be evaluated at any time $t \geq t_1$.

For $m=1$ and in the limit of $p \to \infty$ for a structured mesh (or, equivalently, $A \to 0$) , setting in Eq. (4) the otherwise zero loading function to unity strictly at a single computational grid and at time $t = t_\mathrm{m}$ corresponds to a mathematical description of a point load. Harmonic solid Earth response to a point load sustained on the surface of a radially symmetric layered solid Earth is traditionally computed as the time-dependent Love numbers (Love, 1909; Shida, 1912). We may assemble the Love numbers analytically to determine Green's functions (Appendix A). Given these functions, we can retrieve the solid Earth response signals induced by the loading function with any complexity through direct spatiotemporal convolution:

$$X(\boldsymbol{x},t) = K_X(\alpha,\tau)\ \otimes\ \Delta\mathcal{L}(\boldsymbol{x}',t'), \tag{5}$$

where X is the GRD field of interest [m], K_X is the corresponding Green's function [$\mathrm{m\,kg^{-1}}$], α is the (great circle) distance between the loading position $\boldsymbol{x}'$ and where the response signal is determined $\boldsymbol{x}$, and τ is the time elapsed between the loading time t' and when the response signal is evaluated t (Fig. 1). Let ϕ and λ be the geographic latitude and longitude of the evaluation and loading points: $\boldsymbol{x} \equiv (\phi,\lambda)$ and $\boldsymbol{x}' \equiv (\phi',\lambda')$, respectively. Then, the distance between the two points can be written as $\alpha = r\left[2\arcsin\sqrt{\sin^2\left(\frac{|\phi-\phi'|}{2}\right) + \cos\phi\cos\phi'\sin^2\left(\frac{|\lambda-\lambda'|}{2}\right)}\right]$, where r is the Earth's surface radius. Note that $\Delta\mathcal{L}$ in the equation represents the change in load over the preceding interval to the loading time (Fig. 1c).

In the present context, X denotes either the geoid change G [m] or vertical land motion (VLM). In GIA/GRD theory, where sea level change is due to lateral mass exchange between and within land (including Cryosphere) and the ocean, these quantities are directly related to relative sea level (Eq. 2). The geoid is an equipotential surface of Earth's gravity field that coincides with the mean sea level S over the ocean, while VLM represents change in bedrock elevation B (Gregory et al., 2019).

The convolution operator $\otimes$ appearing in Eq. (5) can be straightforwardly evaluated with scientific computational tools. For example, the desired GRD signal X at a given point in space $\boldsymbol{x}_k$ and time t and can be evaluated as follows:

$$X(\boldsymbol{x}_k,t) = \sum_{j=1}^{p}\sum_{i=1}^{m} K_X(\alpha_{k,j},\tau_\mathrm{i})\ \Delta\mathcal{L}(\boldsymbol{x}'_j,t'_\mathrm{i}), \quad \text{for } t'_\mathrm{m} \leq t, \tag{6}$$

with p and m being the total number of loading points in space and time, respectively, and $\tau_\mathrm{i} = t - t'_\mathrm{i}$. The GRD field can be obtained by iterating over discrete points $k \in [1,q]$, where q is the total number of computational nodes (Fig. 1b). For simulations of ice/Earth coupling at centennial timescales, we expect q to be several orders of magnitude larger than m (a direct function of coupling interval, typically 10 years). A more efficient convolution approach could involve retrieving the GRD field induced by a Heaviside load and iterating along the time dimension. Appendix B presents an algorithm for such a scheme.

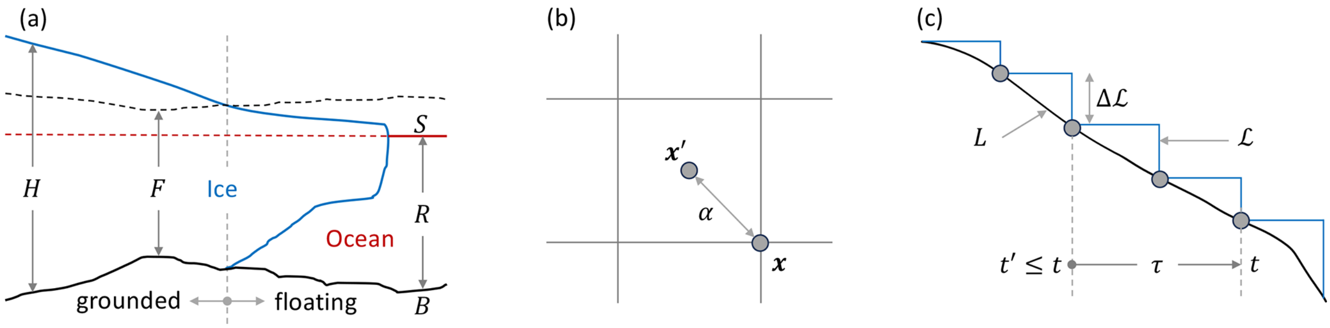

Figure 1. Schematics of the loading function and spatiotemporal grids. **(a)** Longitudinal cross-section of a marine ice sheet as it flows into the ocean. If ice thickness H is larger than the flotation height F, a function of the bedrock topography B and mean sea level S (Eq. 3), it is assumed to be grounded, exerting pressure on the solid Earth's surface. Elsewhere in the ocean (including the floating ice shelves), ocean water (expressed here as the relative sea level $R \equiv S - B$) loads the underlying solid Earth (Eq. 1). **(b)** An example spatial grid illustrating the cell centroid $\boldsymbol{x}'$, where the elemental surface load is applied (Eq. 4), and the vertex $\boldsymbol{x}$, where the desired solid-Earth response signal is evaluated (Eq. 5). The two locations are separated by the great circle distance α. **(c)** Temporal decomposition of the continuous surface load L (diminishing over time in this case) into discrete loading $\mathcal{L}$ using the Heaviside step function (Eq. 4). The discrete loading time t' and the evaluation time t are separated by τ (see Eqs. 5 and 6).

3 Solid Earth Models

A key novelty of the proposed method is the use of a precomputed library of Green's functions that characterize the solid Earth response to applied surface point loads. We calculate time-dependent Love numbers for 644 radially stratified Maxwellian Earth models (Adhikari and Caron, 2024). We also derive corresponding Green's functions, relevant for estimating vertical and horizontal land motion and geoid change. These solutions are based on seismologically constrained density and elastic Earth structure, informed by high-pressure and high-temperature mineral physics (Dziewonski and Anderson, 1981), and incorporate a sufficiently broad range of lithosphere thickness and upper mantle viscosity to investigate solid Earth responses to ice sheet evolution on decadal to centennial timescales, at both individual and multiple drainage basin scales.

Solutions are available for 23×28 combinations of lithosphere thickness and upper mantle viscosity. We linearly sample 23 lithosphere thicknesses between 30 and 250 km at 10 km intervals. Upper mantle viscosity samples include $1 : 9 \times 10^{18}$ Pa s (9 samples), $1 : 9 \times 10^{19}$ Pa s (9 samples), and $1 : 10 \times 10^{20}$ Pa s (10 samples), while the lower mantle viscosity is fixed at 2×10^{22} Pa s for all models. Time-dependent Love numbers and Green's functions are sampled in log-space at 100 snapshots between 0 year (purely elastic signal) and 1000 years. Logarithmic sampling better captures early-time deformation following loading or unloading when the response evolves more rapidly (Figs. 2 and A1). Because the main purpose of this study is to enable centennial-scale simulations, we restrict sampling to the first 1000 years after loading. We further evaluate Green's functions at 500 points along the great-circle distance. We use log-space sampling to capture the signal gradient (a higher gradient in the near field) between 100 m and 20 000 km from the point load (Fig. 2). A 100 m sampling point avoids the inherent singularity in the elastic Green's function at the loading point, while remaining sufficient to capture high-resolution ice load variations associated with grounding line migration and the unpinning of bedrock ridges.

Seismic imaging has provided a three-dimensional view of the crust and upper mantle beneath Antarctica (e.g., Chaput et al., 2014; Lloyd et al., 2020; Lucas et al., 2021; Chua and Lebedev, 2025; Hansen and Emry, 2025), enabling characterization of spatial variations in lithosphere thickness (e.g., An et al., 2015; Wiens et al., 2023; Brown and Fischer, 2025) and mantle viscosity (e.g., Hazzard et al., 2023; Ivins et al., 2023b; Gomez et al., 2024; Lucas et al., 2025). These studies reveal pronounced lateral heterogeneity, indicating that using a single set of solid Earth parameters for the entire ice sheet is not appropriate for coupled simulations (e.g., Coulon et al., 2021; Gomez et al., 2024). Furthermore, tomography-based mantle viscosity estimates exhibit substantial differences among themselves. While GIA-modeled regional uplift rates observed at Global Navigation Satellite Systems (GNSS) bedrock sites are generally consistent with three-dimensional seismic velocity maps, some regions may exhibit significant mismatches between GIA-inferred viscosity and that scaled from tomography (Ivins et al., 2023b). GNSS-based and GIA models that rely on relative sea level records are inherently biased toward coastal regions, where observational constraints are comparatively robust.

Regional estimates of lithosphere thickness (in the sense of mechanical strength used in GRD models) and mantle viscosity have considerable reliance on GNSS trends determined since the mid-to-late 2000s. However, these estimates remain ambiguous, primarily due to uncertainty in the load history (Whitehouse, 2018). When loading chronologies are well-constrained, bounds on upper mantle viscosity η can

Table 1. GIA model- and data-based estimates of lithosphere thickness (LT) and upper mantle viscosity (UMV) relevant for centennial-scale solid Earth response to ice mass changes in Antarctica and Greenland. For each parameter, we provide our recommended values alongside plausible limiting values. See Fig. C1 for the region definition. References: Amalvict et al. (2009) (A09), Adhikari et al. (2021) (A21), Ajourlou et al. (2025) (A25), Bradley et al. (2015) (B15), Barletta et al. (2018) (B18), Ivins et al. (2011) (I11), Khan et al. (2016) (K16), Lewright et al. (2026) (L26), Nield et al. (2014) (N14), Nield et al. (2016) (N16), Näränen et al. (N26), Okuno et al. (2025) (O25), Powell et al. (2020) (P20), Pan et al. (2024) (P24), Scheinert et al. (2006) (S06), Samrat et al. (2020) (S20), Whitehouse et al. (2012) (W12), Wolstencroft et al. (2015) (W15), Weerdesteijn and Conrad (2024) (W24), Zhao et al. (2017) (Z17).

Region	LT [km]	UMV [10^{18} Pa s]	Confidence	References
Northern Peninsula (Graham Land)	50 [30, 80]	10 [1, 90]	high	I11, N14, S20
Southern Peninsula (Palmer Land)	80 [60, 120]	100 [20, 300]	high	W15, Z17
WAIS (Amundsen drainage)	60 [45, 80]	5 [2, 15]	high	B18, P20
WAIS (Ross & Weddell Sea drainage)	80 [60, 120]	300 [100, 500]	medium	W12, B15, N16
EAIS (Amery Ice Shelf & west to Weddell Sea)	120 [50, 250]	600 [500, 1000]	low	S05, O25, N26
EAIS (Amery Ice Shelf & east to Victoria Land)	120 [80, 250]	400 [100, 1000]	low	A09
GrIS (Iceland plume track in eastern Greenland)	40 [30, 100]	10 [1 50]	high	K16, W24, A25
GrIS (Rest of the subcontinent)	100 [60, 200]	70 [10 110]	high	A21, P24, A25, L26

be established. Despite this, uncertainties typically remain on the order of $\log\eta \pm 0.5$ (e.g., Nield et al., 2014; Barletta et al., 2018; Adhikari et al., 2021). This ambiguity is particularly pronounced in regions characterized by low upper mantle viscosity ($\log\eta \leq 19.5$), which are generally associated with slow seismic velocities or relatively young (Neogene) tectonic settings. In these regions, model solutions become highly sensitive to decadal to centennial-scale changes in ice mass load. Under such conditions, the framework proposed here offers particular value by capturing significant solid Earth feedback and enabling efficient exploration of parameter space and uncertainty quantification.

Observational constraints on lithosphere thickness and mantle viscosity from geodetic data are strongest in the Antarctic Peninsula and West Antarctica, whereas substantial uncertainties remain along the sparsely sampled coasts of East Antarctica. Existing constraints are geographically clustered, with studies concentrated in regions such as Graham Land (Nield et al., 2014; Samrat et al., 2020) and the South Shetland Islands (Simms et al., 2012) in the northern Peninsula, Palmer Land (Wolstencroft et al., 2015; Zhao et al., 2017), and key sectors of West Antarctica, including the Amundsen Sea Embayment (Barletta et al., 2018; Powell et al., 2020), Siple Coast (Nield et al., 2016), and the Weddell Sea Embayment (Bradley et al., 2015; Wolstencroft et al., 2015). In contrast, along the extensive East Antarctic coastline, observations are limited to a few regions, such as Dronning Maud Land (Scheinert et al., 2006; Okuno et al., 2025) and the Wilkes Subglacial Embayment (Amalvict et al., 2009), leaving the underlying solid Earth structure comparatively poorly constrained. The extensive coastline from the Amery Basin to George V Coast (spanning 90° in latitude) has an especially acute data shortage (e.g., Scheinert et al., 2026). Across these regions, studies often yield differing estimates of lithosphere thickness and upper mantle viscosity. For example, on the northern Peninsula, some studies suggest weak sensitivity to lithosphere thickness, whereas others infer a thicker lithosphere, yielding comparable viscosity values (Nield et al., 2014; Samrat et al., 2020). Given these discrepancies, prescribing a single, definitive set of regional parameters that accounts for all observations remains challenging. Here, we propose representative parameter sets informed by these studies, as our goal is not to reconcile or discount prior estimates but to provide first-order guidance to ice sheet modelers to enable coupled simulations. Accordingly, we define six sets of solid Earth parameters for Antarctica (Table 1), comprising two regional configurations each for West Antarctica, East Antarctica, and the Peninsula (Fig. C1).

As listed in the table, upper mantle viscosity spans about three orders of magnitude. Figure 2 shows Green's functions for two contrasting Earth structures relevant for marine ice sheet modeling. The Amundsen Sea Embayment, in the West Antarctic Ice Sheet (WAIS), has a thin lithosphere (60 km) and low mantle viscosity (5×10^{18} Pa s). In contrast, the East Antarctic Ice Sheet (EAIS) coasts have a much thicker lithosphere (120 km) and higher viscosity (5×10^{20} Pa s). These differences produce distinctly different responses. In the first model (WAIS-earth), the solid Earth approaches isostatic equilibrium within 250–300 years, with viscous deformation evident in less than a decade. In the East Antarctic model (EAIS-earth), noticeable relaxation develops only after about 100 years of loading.

At the other pole, the Greenland Ice Sheet (GrIS) has received comparatively less attention regarding solid Earth coupling in centennial-scale projections. Here, we provide a brief synthesis of the current state of knowledge of solid Earth structure and parameters, along with a set of recommendations (see Table 1). The data set constraining GIA in Greenland is far more extensive than those for Antarctica (e.g., Khan et al., 2016; Gowan, 2023; Berg et al., 2024; Ajourlou et al., 2025). Seismic imaging reveals three-

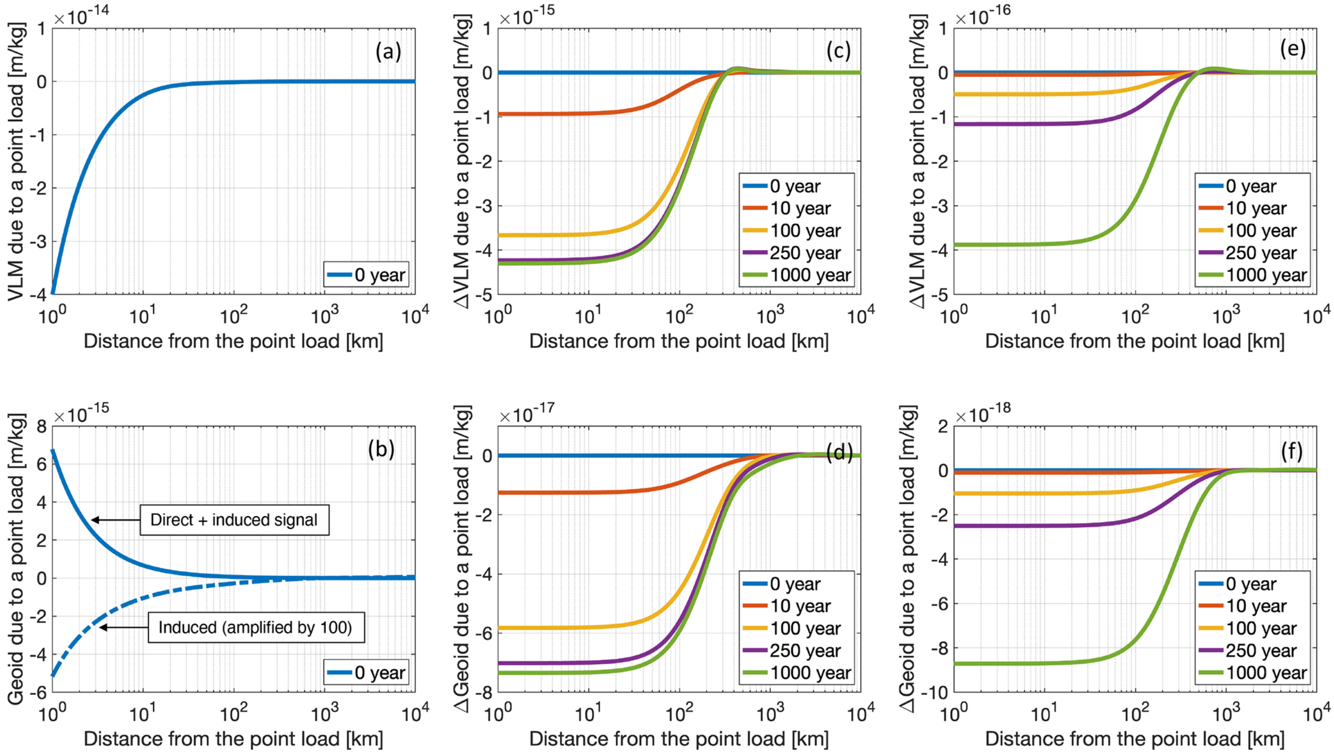

Figure 2. Time-dependent Green's functions for vertical land motion (VLM) and geoid. Panels **(a, b)** show the elastic signals. The direct loading effect (i.e., the first term on the right-hand side of Eq. A2) dominates the geoid signal, as the induced solid Earth response is approximately two orders of magnitude smaller and of opposite sign (panel **b**). Viscous signals, derived here by subtracting the elastic (panels **a**, **b**) from the total viscoelastic solutions, are shown for two contrasting earth models: **(c, d)** WAIS-earth and **(e, f)** EAIS-earth. WAIS-earth represents the viscosity structure beneath the Amundsen Sea Embayment featuring relatively thin lithosphere (60 km) and low upper mantle viscosity (5×10^{18} Pa s). EAIS-earth mimics a plausible structure beneath the East Antarctic coast, with a much thicker lithosphere (120 km) and a higher mantle viscosity (5×10^{20} Pa s). In both cases, the lower mantle viscosity is fixed at 2×10^{22} Pa s.

dimensional variability of lithosphere thickness and mantle viscosity (Milne et al., 2018; Ajourlou et al., 2024), although such structure is generally localized along the Iceland plume track (Khan et al., 2016; Weerdesteijn and Conrad, 2024; Ajourlou et al., 2025). Based on these observations, we recommend adopting two sets of parameters: one for the region impacted by the plume track and the other for the rest of the subcontinent. This distinction is particularly important for accurately modeling major glaciers in central east Greenland, such as Helheim and Kangerdlugssuaq.

Recent efforts to reconcile paleo constraints with modern GNSS observations in regions minimally affected by the Icelandic plume (i.e., most of the subcontinent) support a centennial-scale mantle viscosity on the order of 5×10^{19} Pa s (Adhikari et al., 2021; Lewright et al., 2026). However, constraints on lithosphere thickness remain less well resolved. The inferred viscosity is typically an order of magnitude lower than values commonly adopted in GIA studies targeting millennial timescales (Lecavalier et al., 2014; Milne et al., 2018; Ajourlou et al., 2025). A broadband rheological framework with time-variable viscosity has been proposed to reconcile these differences in viscosity (Paxman et al., 2023), although further investigation is needed to determine its necessity (Pan et al., 2024). For spatial guidance, maps delineating the extent of the plume track region are provided in Khan et al. (2016) and Weerdesteijn and Conrad (2024). Within this area (Fig. C1), we recommend adopting reduced lithosphere thickness and mantle viscosity values, similar to those in the northern Antarctic Peninsula (Table 1).

4 Accuracy of the Proposed Method

We validate the proposed method by comparing example GRD results against self-consistent solutions acquired from simulating the Ice-sheet and Sea-level System Model (ISSM; Adhikari et al., 2016; Houriez et al., 2025). In the latter, self-consistency is sought in the ocean loading and GRD solutions for a given ice loading. We accomplish this by solving the sea level equation (Farrell and Clark, 1976; Milne and Mitrovica, 1998; Kendall et al., 2005; Spada and Melini, 2019) on an unstructured Earth's surface mesh that conserves the total mass of ice and ocean. No regional model, including ours, can resolve self-consistency in global surface loading and the solid Earth response. The critical question is how well the regional model reproduces the self-consistent solutions. For identical representation of ice loading and solid Earth in the regional and global self-consistent models, the difference in predicted GRD solutions stems from the treatment of ocean loading and the rotational feedback. Here, we aim to quantify this difference for the predicted change in VLM and geoid. All regional model solutions include only the ice loading effect. In regions with grounding line migration, we consider only ice above flotation when calculating the load. Rotational feedback is also not accounted for, as shown to be negligible by Larour et al. (2019).

First, we examine the elastic Earth response to the observed trend in Antarctic ice mass change derived from the Gravity Recovery and Climate Experiment (GRACE) and its Follow On (FO) mission data. A key aspect of the load model is the significant mass loss occurring in the Amundsen Sea Sector and Wilkes Land, contrasted by a moderate mass gain in Dronning Maud Land (Fig. 3a). This pattern is also evident in the near field of self-consistent ocean loading (Fig. 3b), where there is a reduction in ocean load (equivalently, relative sea level) near the areas of ice loss and an increase in ocean load near the areas of ice gain. The predicted VLM and geoid fields show minor differences between the regional and global models, suggesting sufficient accuracy of the proposed method. Self-consistent VLM solution is systematically larger (Fig. 3d) due to the reinforcing effect of the ocean load, but this is insignificant in this case of a small sea level change (Fig. 3e). A similarly minor difference is observed in the geoid field (Fig. 3h). This discrepancy appears to be primarily driven by Earth's rotational response, as evidenced by the pronounced degree-2, order-1 pattern in Fig. 3g.

Next, we evaluate the proposed method for two viscoelastic Earth models using a sample of the future evolution of the Antarctic Ice Sheet until 2300. We use precomputed ice sheet model solutions – "experiment 05" of ISMIP6 Antarctica 2300 projections under the Shared Socioeconomic Pathway SSP5-8.5 based on the UKESM climate model (Seroussi et al., 2024; Han et al., 2025) – and load the solid Earth every 10 years between 2010 and 2300 CE. In this load model, the ice sheet mass change does not contribute much to barystatic sea level during the first half of the analysis period (Fig. 4a). The sea level contribution increases rapidly after around 2150, reaching a total change of about 1.5 m. The cumulative ice thickness change suggests substantial mass loss from West Antarctica and along the coastal regions of East Antarctica (Fig. 4b). In contrast, the inland areas of the ice sheet achieve a modest mass gain.

As introduced in the previous section, we consider two Earth models representing plausible structures beneath the Amundsen Sea Embayment (WAIS-earth) and the East Antarctic coasts (EAIS-earth). In the WAIS-earth case, the predicted VLM field exhibits significantly larger amplitudes and more pronounced high wave number features (Fig. 4c) than those in the EAIS-earth case (Fig. 4e). In contrast, the EAIS-earth model yields slightly larger geoid amplitudes (Fig. C2). This difference arises because the geoid signal is primarily governed by the direct effect of surface loads, while the induced solid Earth signal is orders of magnitude smaller (see Fig. 2). Accordingly, the larger amplitudes in the EAIS-earth case reflect reduced solid Earth compensation of the gravitational potential directly associated with the imposed loading (the same for both models). Discrepancies between regional and global model solutions are small (a few percent) for both VLM and geoid fields across all considered solid Earth models. These relative differences remain consistently small over the evaluation period, as illustrated for years 2150 (Fig. C3) and 2300 (Figs. 4 and C2). These differences tend to be larger in regions of strong mass loss and associated bedrock uplift and geoid change. Overall, they primarily reflect the generally reinforcing effect – particularly at long wavelengths – of processes omitted in the regional models, especially ocean loading.

Last, we examine coupled ice/Earth simulations for Thwaites Glacier, building on a recent study by Houriez et al. (2025), to assess the utility of our proposed method in simulating ice sheet dynamics. Their approach uses an anisotropic mesh to capture kilometer-scale grounding line migration and allows for a coupling interval as short as one year. The ice sheet model is initialized by optimizing basal friction and ice rheology to match observed surface velocity (Rignot et al., 2014). It handles basal melt via the PICOP parameterization (Pelle et al., 2019). This approach relies on simulating buoyant plume-driven sub-shelf meltwater circulation within the Potsdam Ice-shelf Cavity Model (PICO) framework (Reese et al., 2018). Model inputs for ocean temperature, salinity, and surface mass balance are based on the Community Earth System Model (CESM) SSP5-8.5 scenario (Danabasoglu et al., 2020). The Earth model complies with the Maxwellian structure constrained by GNSS data (Barletta et al., 2018) and further considers a transient relaxation of the asthenosphere and upper mantle based on the laboratory experiments, the results of which are couched in the formalism of the extended Burgers material (EBM) model (Faul and Jackson, 2015; Ivins et al., 2023a). See Fig. C4 for the characteristic signals of the solid Earth model.

Figure 5 shows predicted grounding line positions and barystatic contributions from a standalone ice sheet simulation and two coupled simulations: one captures the ocean loading effect and rotational feedback (i.e., self-consistent solution), and the other does not (equivalently, the proposed method). The latter coupled model excellently reproduces the self-consistent solutions, capturing the GRD effect on barystatic sea level within 1 % for most of the time. This discrepancy increases up to 2 % by the end of the simulation as a viscous response to ocean loading accumulates over time. It is insignificant compared to the large disparity in the centennial-timescale projections of the Antarctic Ice Sheet (Seroussi et al., 2024). Despite its overall strong perfor-

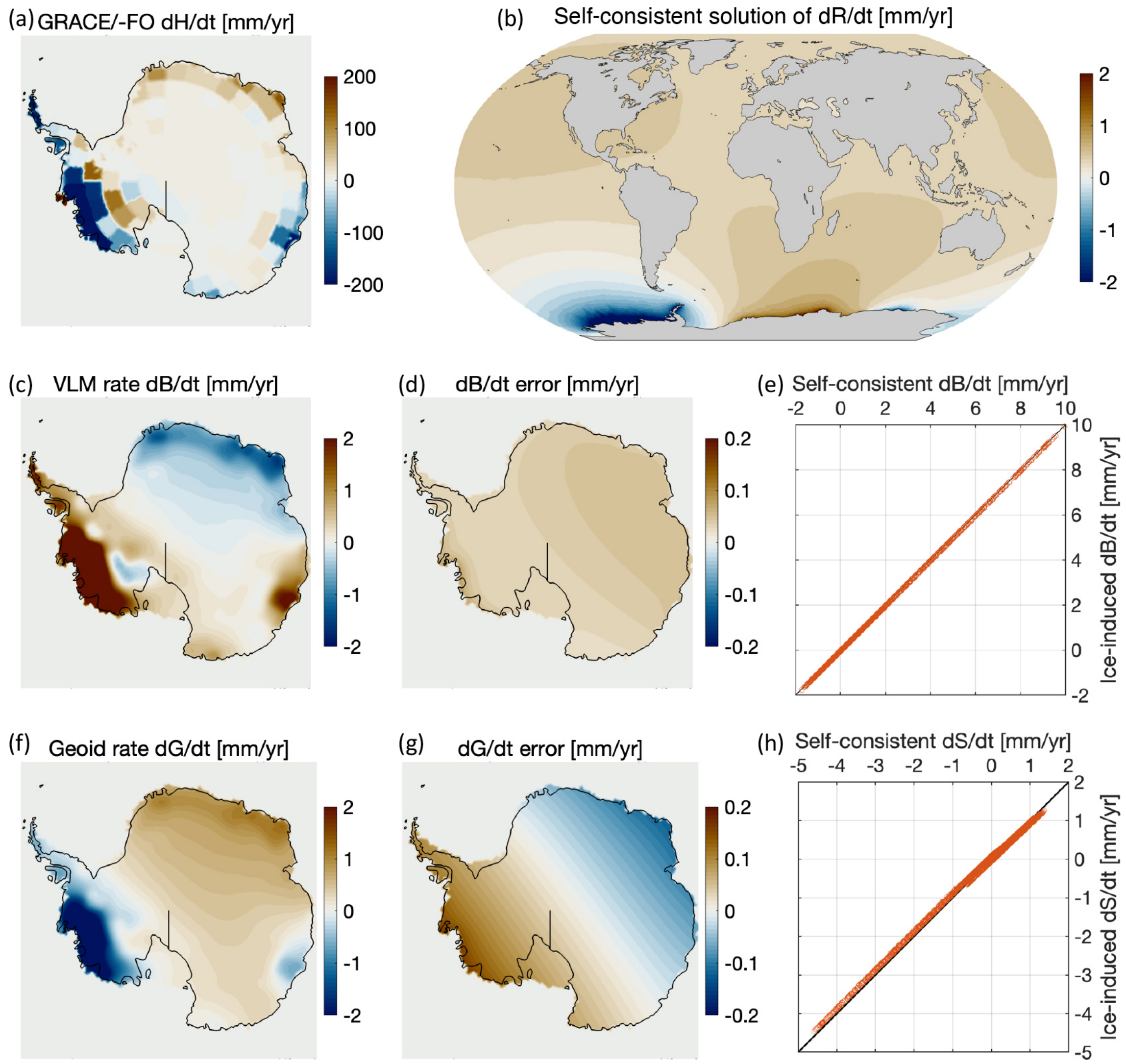

Figure 3. Method accuracy for elastic Earth models. We force the solid Earth by the observed ice load, $\mathrm{d}H/\mathrm{d}t$, derived from the Gravity Recovery and Climate Experiment (GRACE) and its Follow On (FO) mission data over 2002–2024 **(a)**. We quantify the associated self-consistent ocean load, $\mathrm{d}R/\mathrm{d}t$, by solving the sea level equation **(b)**. We use the self-consistent solutions (not shown) for the bedrock topography and geoid change – that capture both the ice and global self-consistent ocean loads (panels **a–b**) – to validate the proposed method. (**c**) Our estimate of vertical land motion (VLM) rate, $\mathrm{d}B/\mathrm{d}t$, induced by the ice load alone (panel **a**). **(d)** The difference in VLM rate between the self-consistent solution and the regional solution over the Antarctic domain (shown in panel **c**). It is at least an order of magnitude smaller than the signal, especially in regions with larger displacement. Indeed, the two solutions appear virtually the same within the ice sheet domain **(e)**, confirming the validity of the proposed method. **(f)–(h)** The same as panels **(c)–(e)**, but for the rate of change in geoid, $\mathrm{d}G/\mathrm{d}t$.

mance, we caution that our regional model may exhibit small but potentially important local deviations from those reported here. Even kilometer-scale offsets in grounding line position near bedrock ridges can influence the timing of unpinning and subsequent ice sheet retreat by several years (e.g., Larour et al., 2019; Houriez et al., 2025).

These examples demonstrate our method's excellent ability to capturing self-consistent solutions within the ice sheet domain. We show that the predicted VLM and geoid fields and their impact on ice dynamics on decadal to centennial timescales are primarily influenced by the direct ice load, which the proposed method can easily handle. The impacts of ocean load and rotational feedback are minimal, although our method can still capture some of these signals. For instance, the ocean load near the ice sheet may be derived and refined iteratively from the VLM and geoid fields, as in the classical sea level solver. However, refined ocean loads may not perfectly align with the self-consistent solutions. Additionally, the centrifugal potential perturbed by ice (and near-field ocean) and its effect on VLM and geoid fields can be

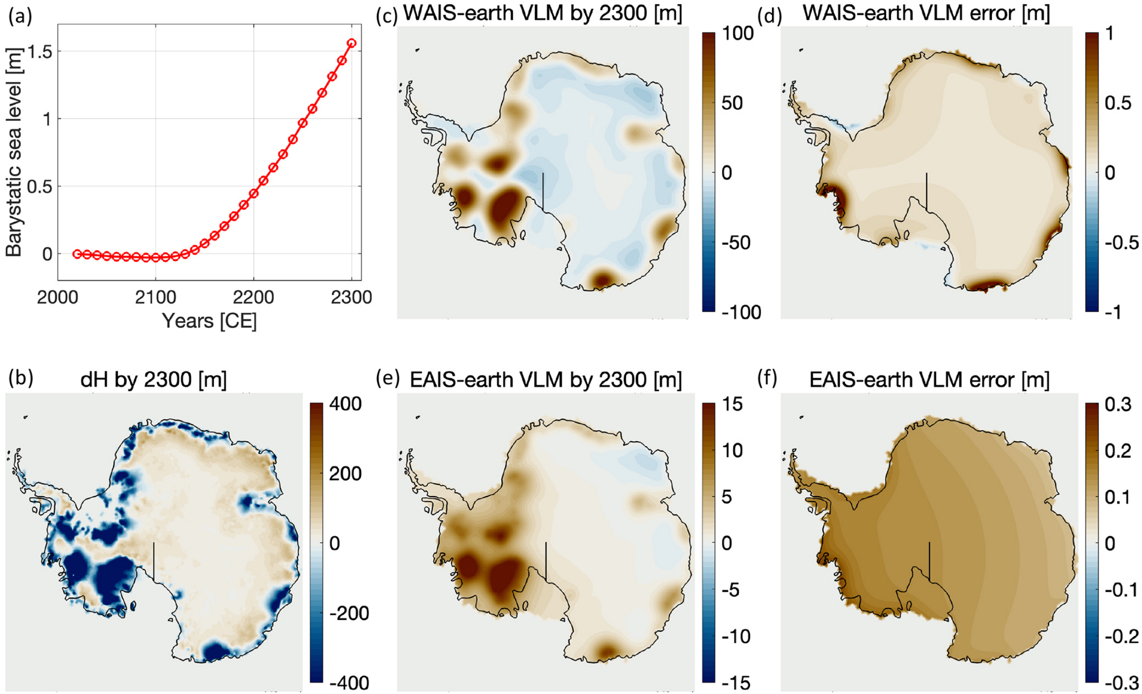

Figure 4. Method accuracy for viscoelastic Earth models. We use the evolving ice thickness data for 2010–2300 based on a solution that applied climate forcings from the recent Ice Sheet Model Intercomparison Project (ISMIP6) (Seroussi et al., 2024) to a coupled model of ice sheet, solid Earth, and sea level (Han et al., 2025): **(a)** Barystatic sea level change at 10-year intervals between 2010 and 2300, and **(b)** the cumulative changes in (thickness equivalent) ice load, dH, over 290 years. **(c)** Total vertical land motion (VLM) by 2300 due to ice load alone, calculated for WAIS-earth using the proposed method. **(d)** Difference between the self-consistent solution (not shown) and the one shown in panel **(c)**. **(e)**–**(f)** Same as panels (c-d), but for EAIS-earth. Regardless of Earth models, VLM errors are about two orders of magnitude smaller than the signals, especially in regions with larger displacement. Geoid fields are shown in Fig. C2. Corresponding results for year 2150 are provided in Fig. C3.

computed semi-analytically. Since the ice load alone captures most of the near-field signals with sufficient accuracy – and given that our primary focus in this paper is on the straightforward retrieval of the leading-order solid Earth signals within the ice sheet model domains – we do not recommend pursuing these higher-order signals, as it may require a more complex workflow for a minimal gain in solution accuracy.

5 Conclusions

We propose a straightforward method that enables ice sheet models to capture realistic solid Earth feedback on decadal to centennial timescales. This method only involves interpolating precomputed Green's functions and performing matrix multiplication with the evolving ice loading. Consequently, it introduces no numerical complexity and does not significantly increase computational costs for ice sheet models. We demonstrate that this method reproduces self-consistent solutions for time-dependent geoid and bedrock topography fields within the ice sheet domain. When the objective is to simplify the ice/Earth coupling strategy while retaining the leading feedback on centennial timescales, we show that ocean loading effects (driven by local or far-field ice mass loss or migrating coastlines) and rotational feedback can be neglected. However, in applications where these processes are essential – such as global glacial isostatic adjustment modeling or interhemispheric ice-sheet interactions – a fully self-consistent solution of the sea level equation remains indispensable (Farrell and Clark, 1976; Milne and Mitrovica, 1998). Our method should therefore not be interpreted as a substitute for a sea level solver.

Recent studies highlight the high sensitivity of solid Earth feedback to ice sheet model resolution and coupling time intervals (e.g., Han et al., 2022; Wan et al., 2022; Houriez et al., 2025; Kodama et al., 2025). In coupled simulations involving a global sea level solver, frequently capturing kilometer-scale features, such as subtle migrations of grounding lines and evolving bedrock ridges, can be challenging. In contrast, our approach – despite the noted limitations – allows ice sheet models to determine the spatiotemporal resolution of solid Earth response signals without added complexity or computational costs. This simplified framework provides a more accessible pathway for ice sheet modelers, including those using standalone systems with limited resources or expertise

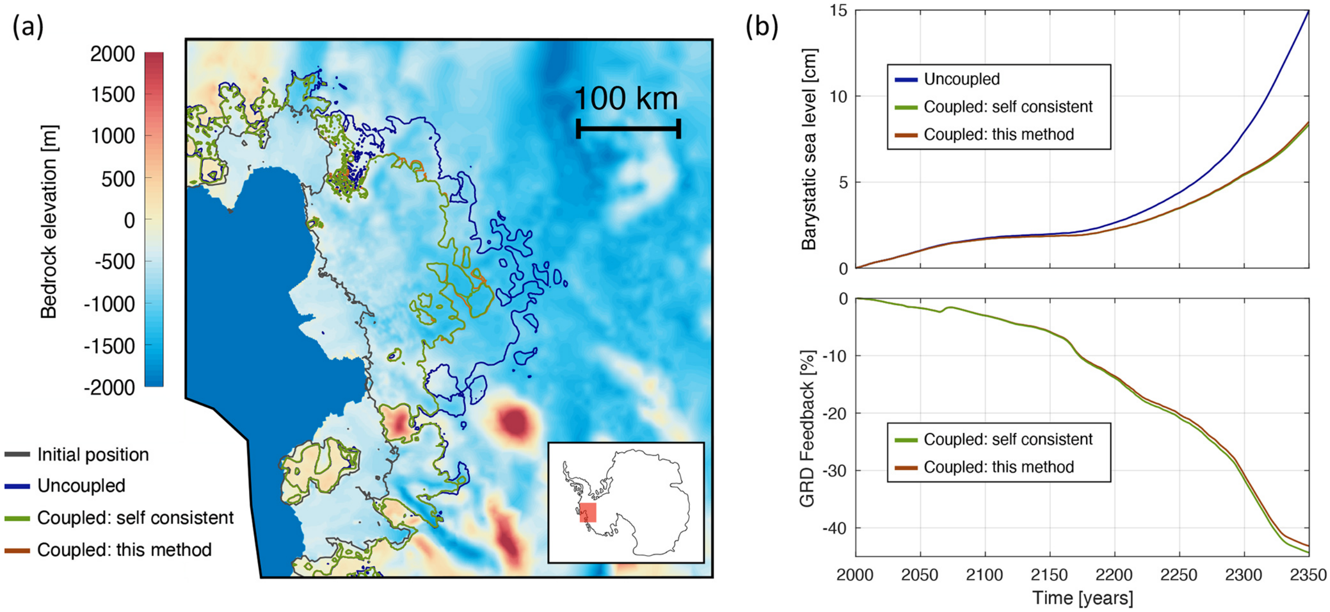

Figure 5. Method accuracy for coupled simulations. We leverage high-resolution coupled simulations for 2000–2350 that try to find consistency in ice sheet dynamics (hence, ice loads), Earth's gravitational, rotational, and deformational (GRD) response, and ocean mass distribution (Houriez et al., 2025). We reproduce key diagnostics of such simulations by coupling the ice sheet and solid Earth with the exclusion of ocean loads and rotational feedback. **(a)** Predicted grounding line positions at 2350 for standalone (uncoupled) ice sheet model and two coupled simulations. (**b**) Barystatic sea level and GRD feedback captured in coupled simulations.

in solid Earth processes, to incorporate a reasonably accurate ice/Earth feedback without significant overhead. Moreover, this reduced-complexity approach enables shorter coupling intervals, yielding more realistic (in certain respects) ice-sheet evolution and projections, or alternatively supports larger ensemble simulations, thereby improving uncertainty quantification and offering a practical advantage for probabilistic sea level projections.

The core idea of our method is to leverage precomputed Green's functions for a radially stratified solid Earth. Open-access tools are available to compute Love numbers and Green's functions for a range of linear viscoelastic models such as Maxwell, Burgers, or extended Burgers materials (e.g., Spada et al., 2004; Caron et al., 2026). An extensive collection of Green's functions for Maxwellian Earth models is already available (Adhikari and Caron, 2024). This library spans a wide range of plausible solid Earth structures, from models with a thin lithosphere and relatively weak upper mantle – such as those inferred geodetically beneath the Amundsen Sea Embayment or the northern Antarctic Peninsula (e.g., Nield et al., 2014; Barletta et al., 2018), as well as from seismic constraints in the Wilkes and Aurora Subglacial Basins (Hansen and Emry, 2025) – to models with cratonic lithosphere and a comparatively stiff mantle, as commonly adopted in glacial isostatic adjustment studies (Lecavalier et al., 2014; Whitehouse, 2018). We aim to further extend this library by performing additional computations for more refined Earth structures, including explicit asthenosphere layering, and more general linear viscoelastic formulations that incorporate transient rheology. Such extensions may be important for accurately modeling ice/Earth feedback at drainage basin scales.

Appendix A: Love Numbers and Green's Functions

The gravitational and deformational response of the solid Earth to a point load applied at its surface is commonly known as the loading Love numbers. These Love numbers play a crucial role in loading studies, including glacial isostatic adjustment theory, under the assumption of radial Earth symmetry. They are derived from the so-called y_i system of equations based on the principles of mass conservation, momentum conservation, and Poisson's equation (Alterman et al., 1959; Peltier, 1974). Here, we leverage the recently coded Love number capability (Caron et al., 2026) of the Ice-sheet and Sea-level System Model (ISSM) that solves the y_i system in the Laplace domain for a suite of linear viscoelastic rheologies, including compressible elastic, Maxwell, Burgers, and extended Burgers materials. It employs the Post-Widder method to convert the spectral solutions to the time domain (Spada and Boschi, 2006). The code has been optimized for parallel performance at high spherical harmonic degrees, targeting to resolve kilometer-scale processes critical for understanding ice sheet and solid Earth interactions (Larour et al., 2019; Houriez et al., 2025). It has been validated against community standards (Spada et al., 2011). The

Love numbers related to radial deformation, $h_\mathrm{n}(t)$, and gravitational potential, $k_\mathrm{n}(t)$, are particularly relevant here. Figure A1 shows example Love numbers for two models representing the solid Earth beneath West and East Antarctica (also see Fig. 2).

Time dependent Love numbers can be assembled to derive the displacement and geoid response to the surface point load (Longman, 1962; Farrell, 1972). These response functions, called Green's functions, may be written as follows:

$$K_\mathrm{B}(\alpha,t) = D\sum_{n=0}^{\infty} h_\mathrm{n}(t)\mathcal{P}_n(\cos\alpha), \tag{A1}$$

$$K_\mathrm{G}(\alpha,t) = D\sum_{n=0}^{\infty} [1+k_\mathrm{n}(t)]\mathcal{P}_n(\cos\alpha). \tag{A2}$$

Here K_B and K_G are Green's functions for bedrock motion (VLM) and geoid, $\mathcal{P}_n$ are Legendre polynomials of degree n, α is the arc length between the location of point load and the location at which the solid Earth response is evaluated (see Sect. 2), and $D = 3/(4\pi r^2\rho_\mathrm{e})$ is the dimensioning constant with ρ_e denoting the mean Earth density. Note that the unity term appearing in the brackets of Eq. (A2) represents the direct effect of the point load on the geoid signal, whereas Love numbers k_n characterize the induced solid Earth response.

We may evaluate the infinite sum in the above equations by truncating the series at a sufficiently high degree, say at $n = N$. A truncation at $N = 10^4$ may be sufficient to capture high wave-number features, such as subtle migration of grounding lines or uplift of subglacial mountains and ridges, critical for understanding the ice/Earth feedback mechanisms (Houriez et al., 2025). However, it appears insufficient to yield accurate and smooth Green's functions, especially in the near field of the loading point (Fig. A2). Noting the asymptotic nature of $h_\mathrm{n}(t) \to h_\infty$ and $nk_\mathrm{n}(t) \to k_\infty$ as $n \to \infty$ (see Fig. A1), Farrell (1972) suggests employing the so-called Kummer's transformation to get rid of these noises. For a sufficiently high-degree truncation, we may invoke $h_\infty \approx h_N$ and $k_\infty \approx Nk_N$ and express Green's functions as follows:

$$K_\mathrm{B}(\alpha,t) \approx D\left\{\frac{h_\infty}{2\sin(\alpha/2)} + \sum_{n=0}^{N}[h_\mathrm{n}(t)-h_\infty]\mathcal{P}_n(\cos\alpha)\right\}, \tag{A3}$$

$$\begin{aligned} K_\mathrm{G}(\alpha,t) \approx D\Bigg\{&\frac{1}{2\sin(\alpha/2)} - k_\infty \ln\left[2\sin(\frac{\alpha}{2})\right] \\ &+ \sum_{n=1}^{N}[k_\mathrm{n}(t) - \frac{k_\infty}{n}]\mathcal{P}_n(\cos\alpha)\Bigg\}. \end{aligned} \tag{A4}$$

As shown in Fig. A2, these expressions behave smoothly and are free from oscillatory artifacts. Adhikari and Caron (2024) deliver such solutions of Green's functions and corresponding Love numbers for numerous Maxwellian Earth models (Sect. 3). Wide spatiotemporal domains and sufficiently dense sampling of these signals across a broad range of radially symmetric Earth structures will enable high-resolution coupled ice/Earth simulations on centennial timescales.

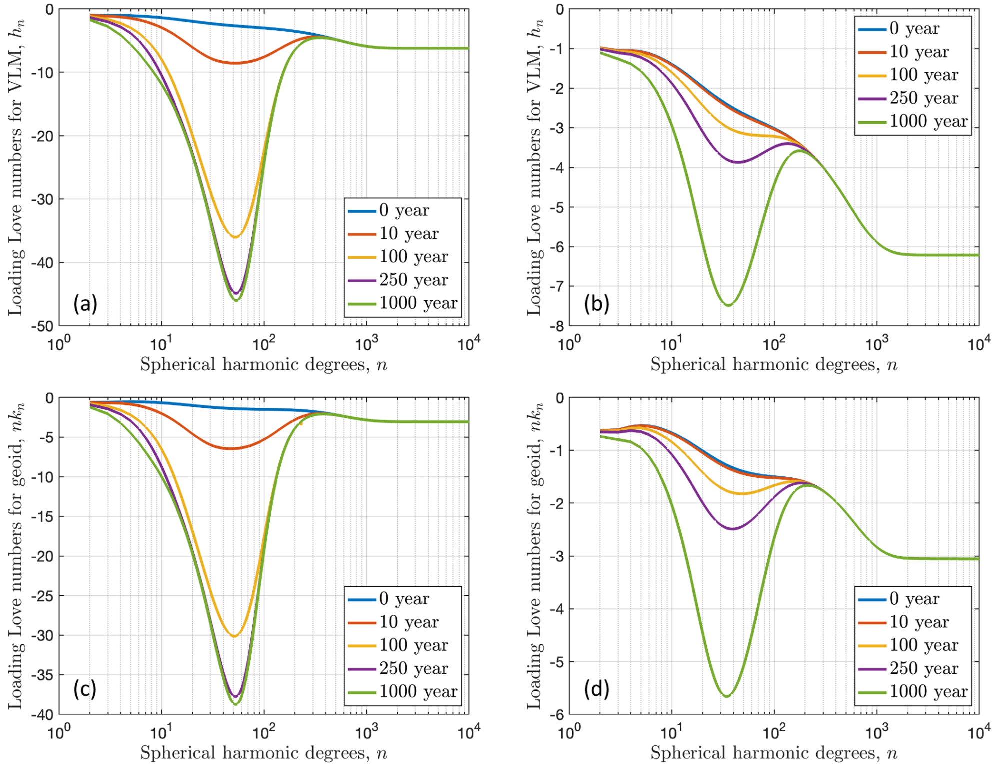

Figure A1. Viscoelastic Love numbers. We show example solutions for two Earth models introduced in Fig. 2: WAIS-earth (left panels) and EAIS-earth (right panels). Love numbers h_n (upper panels) and k_n (lower panels) are relevant for vertical land motion (VLM) and geoid estimation, respectively. Note the asymptotic nature of $h_\mathrm{n}(t)$ and $nk_\mathrm{n}(t)$ towards their respective constants h_∞ and k_∞ as $n \to \infty$. These constants solely depend on the elastic structure of the Earth. For the preliminary reference Earth model (Dziewonski and Anderson, 1981), we find $h_\infty \approx h_{10,000} = -6.214$ and $k_\infty \approx 10^4 k_{10,000} = -3.055$. Notice the different y-axis limits, highlighting the contrasting response signals for the two Earth models. The low viscosity regime in WAIS-earth yields larger-amplitude viscous signals. The thinner lithosphere in this model implies a significant viscous response at high wave numbers ($n \approx 300$ as opposed to $n \approx 200$ in EAIS-earth).

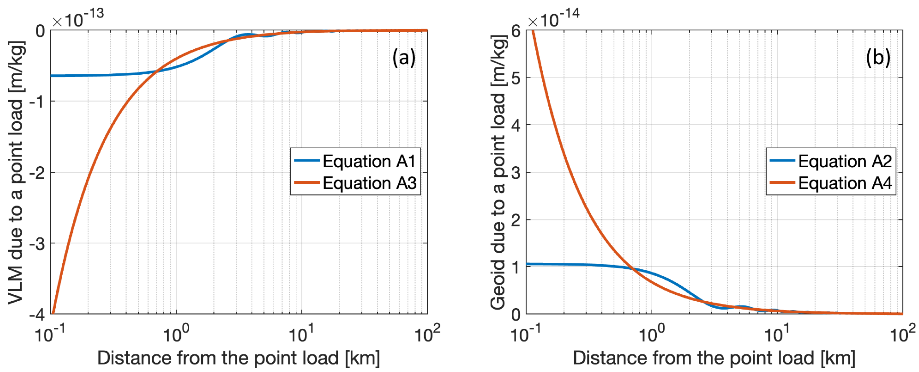

Figure A2. Evaluation of infinite sum in Green's functions. Since evaluating Love numbers up to infinitely large degrees is impractical, we have to truncate the sum appearing in Eqs. (A1) and (A2) at a sufficiently high degree $n = N$. Even if we truncate the sum at $N = 10^4$, Green's functions oscillate in the near field of the applied point load (see blue lines). We handle these oscillations inherent to infinite sums by leveraging the asymptotic nature of Love numbers (see Fig. A1) and using the Kummer transformation that partitions Green's functions into an analytic part whose exact solution exists and the finite sum that yields zero for $n \geq N$. The transformed expressions (Eqs. A3 and A4) accurately capture Green's functions in the near field, hitting the inherent singularity at the loading point (red lines).

Appendix B: A Strategy for Implementing the Proposed Method

Here, we summarize a strategy that may be adapted to evaluate key matrices and convolution. The example we provide is written for Matlab and shall be adapted in any language.

Distance matrix $\alpha(\boldsymbol{x},\boldsymbol{x}')$: We assume that the ice sheet mesh does not evolve in lateral dimensions, allowing us to compute the distance between the loading points (assumed to be elemental centroids) and evaluation points (assumed to be elemental vertices) only once. Let $\boldsymbol{x}_k \equiv (\phi_k, \lambda_k)$ for $k = [1, q]$ and $\boldsymbol{x}'_j \equiv (\phi'_j, \lambda'_j)$ for $j \in [1, p]$ be the geographic coordinates (in radians) of elemental vertices and centroids. The distance matrix will be of $q \times p$ size, where q and p are the total numbers of evaluation and loading points in space (Fig. 1b). We may compute α as follows:

```
for k = 1:q
   dphi = abs(phi2-phi1(k));
   dlam = abs(lambda2-lambda1(k));
   alpha(k,:) = r*2
   *asin(sqrt(sin(dphi/2).^2
   +cos(phi1(k)).*cos(phi2).
   *sin(dlam/2).^2));
end
```

Green's function $K_X(\alpha, \tau)$: We assume that the loading time t' and the evaluation time t are relative to the same reference point and that their discrete representations are known *apriori*. It allows us to predetermine a set of unique non-negative τ, where $\tau = t - t'$ (Figure 1c), and prepare Green's function matrix only once before model run.

```
tau = unique(transpose(t) - t_prime);
tau = tau(tau >= 0);
```

We may now load "greensfunctions.nc" (Adhikari and Caron, 2024) and extract desired solutions for the chosen solid Earth model. All non-defined variables in the following example code are the default variables in the NetCDF file. (We may need to interpolate the solutions further if the desired lithosphere thickness or mantle viscosity does not match those provided.) In this example, we only load Green's functions required for VLM estimation.

```
litho_idx = find(litho_thick
==this_litho); % this_litho:
user defined litho thickness [km]
mant_idx  = find(mant_visco==this_mant);
% this_mant: user defined mantle
viscosity [Pa s]
greens_h_for_desired_earth
 = squeeze(greens_function_h(litho_idx,
 mant_idx,:,:));
greens_h_at_desired_times
= zeros(length(dist),length(tau));
for ii = 1:length(dist)
   greens_input
   = greens_h_for_desired_earth(:,ii);
   greens_h_at_desired_times(ii,:)
   = interp1(eval_times,greens_input,
   tau);
end
```

Finally, we may prepare a three-dimensional Green's function matrix, which will be untouched throughout the coupled model simulations. The following example uses a structure with dynamic variables to access specific Green's functions during convolution easily. The structure "Gvlm" has the same number of fields as the number of τ and each field has a size of $q \times p$, where p and q are once again the total number of elements and vertices.

```
for ii = 1:length(tau)
   time_tag = ['tau',num2str(tau(ii))];
   Gvlm.(time_tag) = interp1(dist,
   greens_h_at_desired_times(:,ii),
   alpha);
end
```

Loading function $\Delta\mathcal{L}(\boldsymbol{x}', t')$: Let m be the total number of Heaviside loads prior to the specific coupling time t (Figure 1c). The loading function $\Delta\mathcal{L}(\boldsymbol{x}', t')$ would have a size of $p \times m$, where p is the number of elements. The ice sheet model computes this function (in units of kg), which we refer to in the following code as "deltaload".

Convolution $X(\boldsymbol{x}, t) = K_X(\alpha, \tau) \otimes \Delta\mathcal{L}(\boldsymbol{x}', t')$: We may perform the spatiotemporal convolution and retrieve the desired GRD signal (vertical land motion "vlm," in this example) as follows.

```
vlm = zeros(q,1);
for ii = 1:m
   tau = t - t_prime(ii);
   time_tag = ['tau',num2str(tau)];
   vlm = vlm + sum(bsxfun(@times,
   Gvlm.(time_tag),transpose
   (deltaload(:,ii))),2);
end
```

Appendix C: Supporting Materials

Here, we include supporting figures (Figs. C1–C4) referenced in the main text.

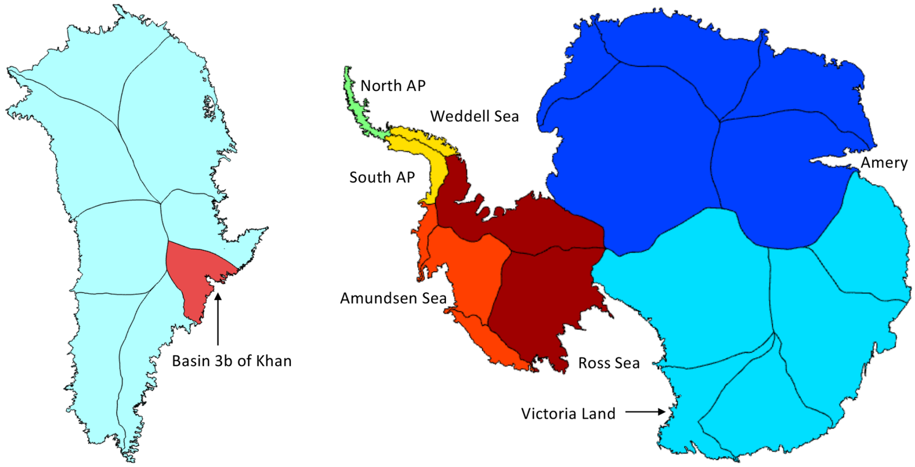

Figure C1. This figure, supplementing Table 1, shows the recommended basin boundaries with distinct solid-Earth parameters: two for Greenland and six for Antarctica. Basin delineations are from Mouginot and Rignot (2019) for Greenland and (Rignot et al., 2013) for Antarctica. The Greenland partition includes basin 3b of Khan et al. (2016), which exhibits anomalously large GNSS uplift signals indicative of the Icelandic plume-affected region.

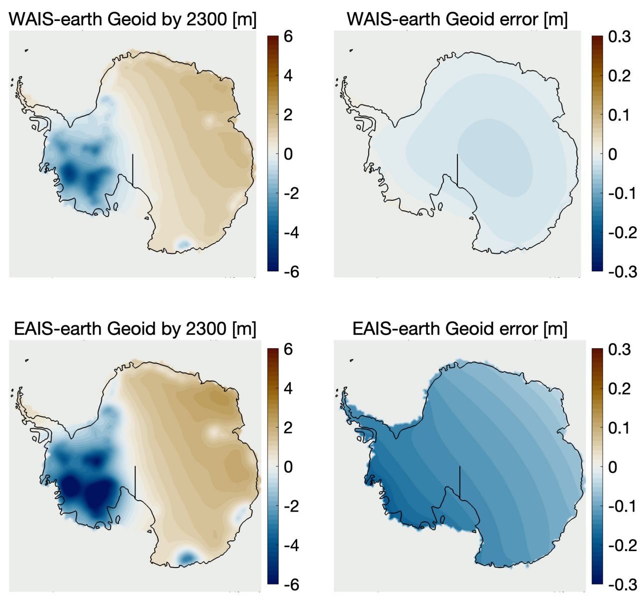

Figure C2. Supplementing Fig. 4, this figure shows geoid fields and their errors relative to self-consistent solutions. The larger amplitudes in the EAIS-earth case reflect reduced solid Earth compensation (compare Fig. 2d versus 2f) of the gravitational potential directly induced by the imposed surface loads (Fig. 2b). The enhanced errors in the EAIS-earth configuration likely arise from the relatively greater influence of direct ocean loading – absent in the regional simulations – compared to the compensating solid Earth response.

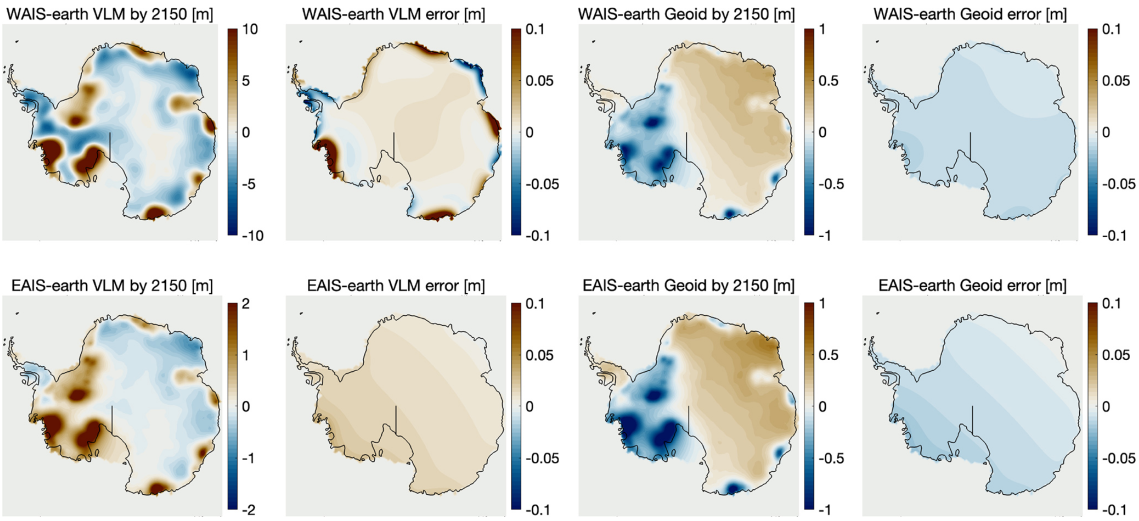

Figure C3. Supplementing Fig. 4, this figure shows VLM and geoid fields at year 2150 and their errors relative to self-consistent solutions.

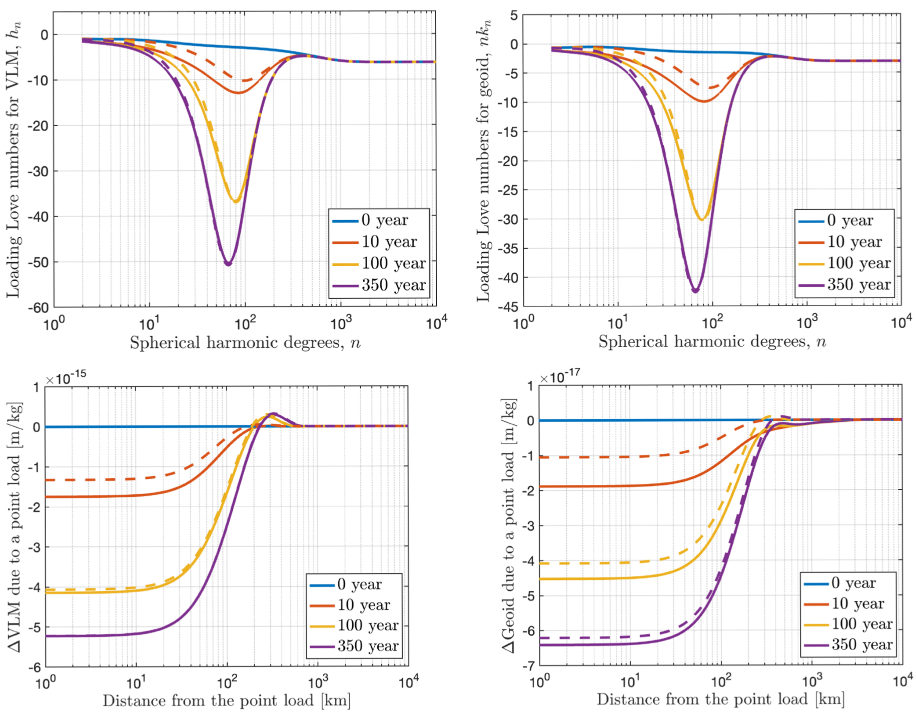

Figure C4. Love numbers and Green's functions for the EBM model (solid lines) used in the coupled simulations (Fig. 5). The upper panels show Love numbers for VLM and geoid change, while the lower panels present the corresponding Green's functions (viscous component). The model consists of a three-layer viscoelastic mantle beneath a 50 km thick lithosphere: a 150 km asthenosphere, an upper mantle extending from 200 to 670 km depth, and a lower mantle. The corresponding Maxwell viscosities are 3.16×10^{18}, 2×10^{20}, and 2×10^{22} Pa s. EBM parameters are held constant across all layers, with $\Delta = 3$, $\alpha = 0.5$, $\tau_H = 7$ years, and $\tau_L = 54$ minutes, and the elastic structure follows PREM (cf. Table 2 of Houriez et al., 2025). Dashed curves denote the equivalent Maxwell model with the same viscosity structure, highlighting the enhanced transient response of the EBM at shorter timescales. It is interesting to note that the transient response has a relatively longer memory in the geoid signals (right panels) than in the VLM (left panels).

Code availability. In Appendix B, we provide an algorithm with some useful Matlab code blocks to facilitate the implementation of the proposed method. Our self-consistent model simulations were conducted using the Ice-sheet and Sea-level System Model (ISSM), an open-access software code available at https://github.com/ISSMteam (last access: 3 September 2026).

Data availability. We provide time-dependent Maxwellian Love numbers and Green's functions for 644 combinations of lithosphere thickness and upper mantle viscosity in https://doi.org/10.7910/DVN/PVDKYI (Adhikari and Caron, 2024).

Author contributions. SA conceived and carried out the research and wrote the first draft of the manuscript. LC helped compute Love numbers. EI led the writing of the Solid Earth Models section. HH contributed to validating the proposed method. LH and EL performed coupled simulations. All authors reviewed, edited, and approved the manuscript.

Competing interests. The contact author has declared that none of the authors has any competing interests.

Disclaimer. Publisher's note: Copernicus Publications remains neutral with regard to jurisdictional claims made in the text, published maps, institutional affiliations, or any other geographical representation in this paper. The authors bear the ultimate responsibility for providing appropriate place names. Views expressed in the text are those of the authors and do not necessarily reflect the views of the publisher.

Acknowledgements. This research was conducted at the Jet Propulsion Laboratory, California Institute of Technology, under a contract with the National Aeronautics and Space Administration (NASA). This work was inspired by discussions within the ISMIP7 GIA & Sea-level Focus Group. L.H. wishes to acknowledge advising from Professors Fischer and Darve as well as the support of the Stanford Data Science Scholars.

Financial support. Funding support was provided by NASA's Sea-level Change Team (N-SLCT), Earth Surface and Interior (ESI) Focus Area, the Modeling, Analysis, and Prediction (MAP) Program, and the Cryosphere Sciences Program.

Review statement. This paper was edited by Elisa Mantelli and reviewed by Volker Klemann and two anonymous referees.

References

Adhikari, S. and Caron, L.: Love numbers and Greens functions for a suite of radially-symmetric stratified Maxwell Earth, Harvard Dataverse [data set], https://doi.org/10.7910/DVN/PVDKYI, 2024.

Adhikari, S., Ivins, E. R., Larour, E., Seroussi, H., Morlighem, M., and Nowicki, S.: Future Antarctic bed topography and its implications for ice sheet dynamics, Solid Earth, 5, 569–584, https://doi.org/10.5194/se-5-569-2014, 2014.

Adhikari, S., Ivins, E. R., and Larour, E.: ISSM-SESAW v1.0: mesh-based computation of gravitationally consistent sea-level and geodetic signatures caused by cryosphere and climate driven mass change, Geosci. Model Dev., 9, 1087–1109, https://doi.org/10.5194/gmd-9-1087-2016, 2016.

Adhikari, S., Milne, G. A., Caron, L., Khan, S. A., Kjeldsen, K. K., Nilsson, J., Larour, E., and Ivins, E. R.: Decadal to Centennial Timescale Mantle Viscosity Inferred From Modern Crustal Uplift Rates in Greenland, Geophys. Res. Lett., 48, e2021GL094040, https://doi.org/10.1029/2021GL094040, 2021.

Ajourlou, P., Darbyshire, F., Audet, P., and Milne, G. A.: Structure of the crust and upper mantle in Greenland and northeastern Canada: insights from anisotropic Rayleigh-wave tomography, Geophys. J. Int., 239, 329–350, https://doi.org/10.1093/gji/ggae269, 2024.

Ajourlou, P., Milne, G. A., Love, R., Afonso, J. C., Salajegheh, F., Latychev, K., Kjeldsen, K. K., Lepipas, A., Martos, Y. M., and Woodroffe, S. A.: Upper mantle temperatures illuminate the Iceland hotspot track and understanding of ice – Earth interactions in Greenland, P. Natl. Acad. Sci. USA, 122, e2504752122, https://doi.org/10.1073/pnas.2504752122, 2025.

Albrecht, T., Bagge, M., and Klemann, V.: Feedback mechanisms controlling Antarctic glacial-cycle dynamics simulated with a coupled ice sheet–solid Earth model, The Cryosphere, 18, 4233–4255, https://doi.org/10.5194/tc-18-4233-2024, 2024.

Alterman, Z., Jarosch, H., Pekeris, C. L., and Jeffreys, H.: Oscillations of the earth, P. Roy. Soc. Lond. A Mat., 252, 80–95, https://doi.org/10.1098/rspa.1959.0138, 1959.

Amalvict, M., Willis, P., Wöppelmann, G., Ivins, E. R., Bouin, M.-N., Testut, L., and Hinderer, J.: Isostatic stability of the East Antarctic station Dumont d'Urville from long-term geodetic observations and geophysical models, Polar Res., 28, 193–202, https://doi.org/10.3402/polar.v28i2.6112, 2009.

An, M., Wiens, D. A., Zhao, Y., Feng, M., Nyblade, A., Kanao, M., Li, Y., Maggi, A., and Lévêque, J.-J.: Temperature, lithosphere-asthenosphere boundary, and heat flux beneath the Antarctic Plate inferred from seismic velocities, J. Geophys. Res.-Sol. Ea., 120, 8720–8742, https://doi.org/10.1002/2015JB011917, 2015.

Barletta, V. R., Bevis, M., Smith, B. E., Wilson, T., Brown, A., Bordoni, A., Willis, M., Khan, S. A., Rovira-Navarro, M., Dalziel, I., Smalley, R., Kendrick, E., Konfal, S., Caccamise, D. J., Aster, R. C., Nyblade, A., and Wiens, D. A.: Observed rapid bedrock uplift in Amundsen Sea Embayment promotes ice-sheet stability, Science, 360, 1335–1339, https://doi.org/10.1126/science.aao1447, 2018.

Berg, D., Barletta, V. R., Hassan, J., Lippert, E. Y. H., Colgan, W., Bevis, M., Steffen, R., and Khan, S. A.: Vertical Land Motion Due To Present-Day Ice Loss From Greenland's and Canada's Peripheral Glaciers, Geophys. Res. Lett., 51, e2023GL104851, https://doi.org/10.1029/2023GL104851, 2024.

Bradley, S. L., Hindmarsh, R. C. A., Whitehouse, P. L., Bentley, M. J., and King, M. A.: Low post-glacial rebound rates in the Weddell Sea due to late Holocene ice-sheet readvance, Earth Planet. Sc. Lett., 413, 79–89, https://doi.org/10.1016/j.epsl.2014.12.039, 2015.

Brown, S. E. and Fischer, K. M.: Investigating the Antarctic Lithosphere Through Sp Receiver Function Analysis, Geochem. Geophy. Geosy., 26, e2025GC012268, https://doi.org/10.1029/2025GC012268, 2025.

Caron, L., Ivins, E., Larour, E., Adhikari, S., and Métivier, L.: Love number computation within the Ice-sheet and Sea-level System Model (ISSM v4.24), Geosci. Model Dev., 19, 4031–4054, https://doi.org/10.5194/gmd-19-4031-2026, 2026.

Chaput, J., Aster, R. C., Huerta, A., Sun, X., Lloyd, A., Wiens, D., Nyblade, A., Anandakrishnan, S., Winberry, J. P., and Wilson, T.: The crustal thickness of West Antarctica, J. Geophys. Res.-Sol. Ea., 119, 378–395, https://doi.org/10.1002/2013JB010642, 2014.

Chua, E. L. and Lebedev, S.: Waveform tomography of the Antarctic Plate, Geophys. J. Int., 241, 219–240, https://doi.org/10.1093/gji/ggaf041, 2025.

Coonin, A. N., Parazin, B., Lau, H. C. P., and Gomez, N.: West Antarctic Ice Retreat Temporarily Halted with Transient Rheology in Future Climate Projections, EGUsphere [preprint], https://doi.org/10.5194/egusphere-2026-2172, 2026.

Coulon, V., Bulthuis, K., Whitehouse, P. L., Sun, S., Haubner, K., Zipf, L., and Pattyn, F.: Contrasting Response of West and East Antarctic Ice Sheets to Glacial Isostatic Adjustment, J. Geophys. Res.-Earth, 126, e2020JF006003, https://doi.org/10.1029/2020JF006003, 2021.

Danabasoglu, G., Lamarque, J.-F., Bacmeister, J., Bailey, D. A., DuVivier, A. K., Edwards, J., Emmons, L. K., Fasullo, J., Garcia, R., Gettelman, A., Hannay, C., Holland, M. M., Large, W. G., Lauritzen, P. H., Lawrence, D. M., Lenaerts, J. T. M., Lindsay, K., Lipscomb, W. H., Mills, M. J., Neale, R., Oleson, K. W., Otto-Bliesner, B., Phillips, A. S., Sacks, W., Tilmes, S., van Kampenhout, L., Vertenstein, M., Bertini, A., Dennis, J., Deser, C., Fischer, C., Fox-Kemper, B., Kay, J. E., Kinnison, D., Kushner, P. J., Larson, V. E., Long, M. C., Mickelson, S., Moore, J. K., Nienhouse, E., Polvani, L., Rasch, P. J., and Strand, W. G.: The Community Earth System Model Version 2 (CESM2), J. Adv. Model. Earth Sy., 12, e2019MS001916, https://doi.org/10.1029/2019MS001916, 2020.

Dziewonski, A. M. and Anderson, D. L.: Preliminary reference Earth model, Physi. Earth Planet. In., 25, 297–356, https://doi.org/10.1016/0031-9201(81)90046-7, 1981.

Farrell, W. E.: Deformation of the Earth by surface loads, Rev. Geophys., 10, 761–797, https://doi.org/10.1029/RG010i003p00761, 1972.

Farrell, W. E. and Clark, J. A.: On Postglacial Sea Level, Geophys. J. Int., 46, 647–667, https://doi.org/10.1111/j.1365-246X.1976.tb01252.x, 1976.

Faul, U. and Jackson, I.: Transient Creep and Strain Energy Dissipation: An Experimental Perspective, Annu. Rev. Earth Pl. Sc., 43, 541–569, https://doi.org/10.1146/annurev-earth-060313-054732, 2015.

Gomez, N., Pollard, D., Mitrovica, J. X., Huybers, P., and Clark, P. U.: Evolution of a coupled marine ice sheet–sea level model, J. Geophys. Res.-Earth, 117, https://doi.org/10.1029/2011JF002128, 2012.

Gomez, N., Weber, M. E., Clark, P. U., Mitrovica, J. X., and K., H.: Antarctic ice dynamics amplified by Northern Hemisphere sea-level forcing, Nature, 587, https://doi.org/10.1038/s41586-020-2916-2, 2020.

Gomez, N., Yousefi, M., Pollard, D., DeConto, R. M., Sadai, S., Lloyd, A., Nyblade, A., Wiens, D. A., Aster, R. C., and Wilson, T.: The influence of realistic 3D mantle viscosity on Antarctica's contribution to future global sea levels, Science Advances, 10, eadn1470, https://doi.org/10.1126/sciadv.adn1470, 2024.

Gowan, E. J.: Paleo sea-level indicators and proxies from Greenland in the GAPSLIP database and comparison with modelled sea level from the PaleoMIST ice-sheet reconstruction, GEUS Bulletin, 53, https://doi.org/10.34194/geusb.v53.8355, 2023.

Gregory, J. M., Griffies, S. M., Hughes, C. W., Lowe, J. A., Church, J. A., Fukutomi, Y., Gomez, N., Kopp, R. E., Landerer, F. W., Le Cozannet, G., Ponte, R. M., Stammer, D., Tamisiea, M. E., Thompson, P. R., von Schuckmann, K., and Widmann, M.: Concepts and Terminology for Sea Level: Mean, Variability and Change, Both Local and Global, Surv. Geophys., 40, 1251–1289, https://doi.org/10.1007/s10712-019-09525-z, 2019.

Han, H. K., Gomez, N., and Wan, J. X. W.: Capturing the interactions between ice sheets, sea level and the solid Earth on a range of timescales: a new "time window" algorithm, Geosci. Model Dev., 15, 1355–1373, https://doi.org/10.5194/gmd-15-1355-2022, 2022.

Han, H. K., Hoffman, M., Asay-Davis, X., Hillebrand, T. R., and Perego, M.: Improving Projections of Antarctic Ice Sheet Contribution to Sea-Level Change Through 2300 by Capturing Gravitational, Rotational, and Deformational Effects, J. Geophys. Res.-Earth, 130, e2025JF008388, https://doi.org/10.1029/2025JF008388, 2025.

Hansen, S. E. and Emry, E. L.: East Antarctic tectonic basin structure and its implications for ice-sheet modeling and sea-level projections, Communications Earth & Environment, 6, 138, https://doi.org/10.1038/s43247-025-02140-4, 2025.

Hazzard, J. A. N., Richards, F. D., Goes, S. D. B., and Roberts, G. G.: Probabilistic Assessment of Antarctic Thermomechanical Structure: Impacts on Ice Sheet Stability, J. Geophys. Res.-Sol. Ea., 128, e2023JB026653, https://doi.org/10.1029/2023JB026653, 2023.

Houriez, L., Larour, E., Caron, L., Schlegel, N.-J., Adhikari, S., Ivins, E., Pelle, T., Seroussi, H., Darve, E., and Fischer, M.: Reinforced ridges in Thwaites Glacier yield insights into resolution requirements for coupled ice sheet and solid Earth models, The Cryosphere, 19, 4355–4372, https://doi.org/10.5194/tc-19-4355-2025, 2025.

Ivins, E. R. and James, T. S.: Simple models for late Holocene and present-day Patagonian glacier fluctuations and predictions of a geodetically detectable isostatic response, Geophys. J. Int., 138, 601–624, https://doi.org/10.1046/j.1365-246x.1999.00899.x, 1999.

Ivins, E. R., Watkins, M. M., Yuan, D.-N., Dietrich, R., Casassa, G., and Rülke, A.: On-land ice loss and Glacial Isostatic Adjustment at the Drake Passage: 2003–2009, J. Geophys. Res.-Sol. Ea., 116, https://doi.org/10.1029/2010JB007607, 2011.

Ivins, E., Caron, L., and Adhikari, S.: Anthropocene isostatic adjustment on an anelastic mantle, J. Geodesy, 97, 1043–1049, https://doi.org/10.1007/s00190-023-01781-7, 2023a.

Ivins, E. R., van der Wal, W., Wiens, D. A., Lloyd, A. J., and Caron, L.: Antarctic upper mantle rheology, Geological Society, London, Memoirs, 56, 267–294, https://doi.org/10.1144/M56-2020-19, 2023b.

Kendall, R. A., Mitrovica, J. X., and Milne, G. A.: On post-glacial sea level – II. Numerical formulation and comparative results on spherically symmetric models, Geophys. J. Int., 161, 679–706, https://doi.org/10.1111/j.1365-246X.2005.02553.x, 2005.

Khan, S. A. et al.: Geodetic measurements reveal similarities between post–Last Glacial Maximum and present-day mass loss from the Greenland ice sheet, Science Advances, 2, e1600931, https://doi.org/10.1126/sciadv.1600931, 2016.

Kodama, S. T., Pico, T., Robel, A. A., Christian, J. E., Gomez, N., Vigilia, C., Powell, E., Gagliardi, J., Tulaczyk, S., and Blackburn, T.: Impact of glacial isostatic adjustment on zones of potential grounding line persistence in the Ross Sea Embayment (Antarctica) since the Last Glacial Maximum, The Cryosphere, 19, 2935–2948, https://doi.org/10.5194/tc-19-2935-2025, 2025.

Konrad, H., Sasgen, I., Pollard, D., and Klemann, V.: Potential of the solid-Earth response for limiting long-term West Antarctic Ice Sheet retreat in a warming climate, Earth Planet. Sc. Lett., 432, 254–264, https://doi.org/10.1016/j.epsl.2015.10.008, 2015.

Konrad, H., Sasgen, I., Klemann, V., Thoma, M., Grosfeld, K., and Martinec, Z.: Sensitivity of Grounding-Line Dynamics to Viscoelastic Deformation of the Solid-Earth in an Idealized Scenario, Polarforschung, 85, 89–99, https://doi.org/10.2312/polfor.2016.005, 2016.

Kreuzer, M., Albrecht, T., Nicola, L., Reese, R., and Winkelmann, R.: Bathymetry-constrained impact of relative sea-level change on basal melting in Antarctica, The Cryosphere, 19, 1181–1203, https://doi.org/10.5194/tc-19-1181-2025, 2025.

Larour, E., Seroussi, H., Adhikari, S., Ivins, E., Caron, L., Morlighem, M., and Schlegel, N.: Slowdown in Antarctic mass loss from solid Earth and sea-level feedbacks, Science, 364, eaav7908, https://doi.org/10.1126/science.aav7908, 2019.

Lecavalier, B. S., Milne, G. A., Simpson, M. J., Wake, L., Huybrechts, P., Tarasov, L., Kjeldsen, K. K., Funder, S., Long, A. J., Woodroffe, S., Dyke, A. S., and Larsen, N. K.: A model of Greenland ice sheet deglaciation constrained by observations of relative sea level and ice extent, Quaternary Sci. Rev., 102, 54–84, https://doi.org/10.1016/j.quascirev.2014.07.018, 2014.

Lewright, L., Austermann, J., Piecuch, C. G., Adhikari, S., Davis, J. L., Milne, G. A., and Paxman, G. J. G.: Projections of 21st-century sea-level fall along coastal Greenland, Nat. Commun., 17, 353, https://doi.org/10.1038/s41467-025-68182-6, 2026.

Lin, Y., Whitehouse, P. L., Valentine, A. P., and Woodroffe, S. A.: GEORGIA: A Graph Neural Network Based EmulatOR for Glacial Isostatic Adjustment, Geophysical Res. Lett., 50, e2023GL103672, https://doi.org/10.1029/2023GL103672, 2023.

Lingle, C. S. and Clark, J. A.: A numerical model of interactions between a marine ice sheet and the solid earth: Application to a West Antarctic ice stream, J. Geophys. Res.-Oceans, 90, 1100–1114, https://doi.org/10.1029/JC090iC01p01100, 1985.

Lloyd, A. J., Wiens, D. A., Zhu, H., Tromp, J., Nyblade, A. A., Aster, R. C., Hansen, S. E., Dalziel, I. W. D., Wilson, T., Ivins, E. R., and O'Donnell, J. P.: Seismic Structure of the Antarctic Upper Mantle Imaged with Adjoint Tomography, J. Geophys. Res.-Sol. Ea., 125, https://doi.org/10.1029/2019JB017823, 2020.

Longman, I. M.: A Green's function for determining the deformation of the Earth under surface mass loads: 1. Theory, J. Geophys. Res., 67, 845–850, https://doi.org/10.1029/JZ067i002p00845, 1962.

Love, A. E. H.: The yielding of the earth to disturbing forces, P. R. Soc. Lond. A-Conta., 82, 73–88, https://doi.org/10.1098/rspa.1909.0008, 1909.

Love, R., Milne, G. A., Ajourlou, P., Parang, S., Tarasov, L., and Latychev, K.: A fast surrogate model for 3D Earth glacial isostatic adjustment using Tensorflow (v2.8.0) artificial neural networks, Geosci. Model Dev., 17, 8535–8551, https://doi.org/10.5194/gmd-17-8535-2024, 2024.

Lucas, E. M., Nyblade, A. A., Lloyd, A. J., Aster, R. C., Wiens, D. A., O'Donnell, J. P., Stuart, G. W., Wilson, T. J., Dalziel, I. W. D., Winberry, J. P., and Huerta, A. D.: Seismicity and Pn Velocity Structure of Central West Antarctica, Geochem. Geophy. Geosy., 22, e2020GC009471, https://doi.org/10.1029/2020GC009471, 2021.

Lucas, E. M., Gomez, N., and Wilson, T.: The impact of regional-scale upper-mantle heterogeneity on glacial isostatic adjustment in West Antarctica, The Cryosphere, 19, 2387–2405, https://doi.org/10.5194/tc-19-2387-2025, 2025.

Meur, E. L. and Huybrechts, P.: A comparison of different ways of dealing with isostasy: examples from modeling the Antarctic ice sheet during the last glacial cycle, Ann. Glaciol., 23, 309–317, 1996.

Milne, G. A. and Mitrovica, J. X.: Postglacial sea-level change on a rotating Earth, Geophys. J. Int., 133, 1–19, https://doi.org/10.1046/j.1365-246X.1998.1331455.x, 1998.

Milne, G. A., Latychev, K., Schaeffer, A., Crowley, J. W., Lecavalier, B. S., and Audette, A.: The influence of lateral Earth structure on glacial isostatic adjustment in Greenland, Geophys. J. Int., 214, 1252–1266, https://doi.org/10.1093/gji/ggy189, 2018.

Mouginot, J. and Rignot, E.: Glacier catchments/basins for the Greenland Ice Sheet, Dryad [data set], https://doi.org/10.7280/D1WT11, 2019.

Näränen, J., Mäkinen, J., Nordman, M., and Raja-Halli, A.: Three Decades of Repeated Absolute Gravity Measurements at the Finnish Antarctic Research Station Aboa, Pure Appl. Geophys., 183, 137–157, https://doi.org/10.1007/s00024-025-03868-y.

Nield, G. A., Barletta, V. R., Bordoni, A., King, M. A., Whitehouse, P. L., Clarke, P. J., Domack, E., Scambos, T. A., and Berthier, E.: Rapid bedrock uplift in the Antarctic Peninsula explained by viscoelastic response to recent ice unloading, Earth Planet. Sc. Lett., 397, 32–41, https://doi.org/10.1016/j.epsl.2014.04.019, 2014.

Nield, G. A., Whitehouse, P. L., King, M. A., and Clarke, P. J.: Glacial isostatic adjustment in response to changing late Holocene behaviour of ice streams on the Siple Coast, West Antarctica, Geophys. J. Int., 205, 1–21, https://doi.org/10.1093/gji/ggv532, 2016.

Okuno, J., Hattori, A., Doi, K., et al.: Mid Holocene rapid thinning and rethickening of the East Antarctic ice sheet suggested by glacial isostatic adjustment, Scientific Reports, 15, 40207, https://doi.org/10.1038/s41598-025-24176-4, 2025.

Pan, L., Mitrovica, J. X., Milne, G. A., Hoggard, M. J., and Woodroffe, S. A.: Timescales of glacial isostatic adjustment in

Greenland: is transient rheology required?, Geophys. J. Int., 237, 989–995, https://doi.org/10.1093/gji/ggae095, 2024.

Paxman, G. J. G., Lau, H. C., Austermann, J., Holtzman, B. K., and Havlin, C.: Inference of the timescale-dependent apparent viscosity structure in the upper mantle beneath Greenland, AGU Advances, 4, e2022AV000751, https://doi.org/10.1029/2022AV000751, 2023.

Pelle, T., Morlighem, M., and Bondzio, J. H.: Brief communication: PICOP, a new ocean melt parameterization under ice shelves combining PICO and a plume model, The Cryosphere, 13, 1043–1049, https://doi.org/10.5194/tc-13-1043-2019, 2019.

Peltier, W. R.: The impulse response of a Maxwell Earth, Rev. Geophys., 12, 649–669, https://doi.org/10.1029/RG012i004p00649, 1974.

Powell, E., Gomez, N., Hay, C., Latychev, K., and Mitrovica, J. X.: Viscous effects in the solid earth response to modern Antarctic ice mass flux: Implications for geodetic studies of WAIS stability in a warming world, J. Climate, 33, 443–459, https://doi.org/10.1175/JCLI-D-19-0479.1, 2020.

Reese, R., Albrecht, T., Mengel, M., Asay-Davis, X., and Winkelmann, R.: Antarctic sub-shelf melt rates via PICO, The Cryosphere, 12, 1969–1985, https://doi.org/10.5194/tc-12-1969-2018, 2018.

Rignot, E., Jacobs, S., Mouginot, J., and Scheuchl, B.: Ice Shelf Melting Around Antarctica, Science, 341, 266–270, https://doi.org/10.1126/science.1235798, 2013.

Rignot, E., Mouginot, J., Morlighem, M., Seroussi, H., and Scheuchl, B.: Widespread, rapid grounding line retreat of Pine Island, Thwaites, Smith, and Kohler glaciers, West Antarctica, from 1992 to 2011, Geophys. Res. Lett., 41, 3502–3509, https://doi.org/10.1002/2014GL060140, 2014.

Samrat, N. H., King, M. A., Watson, C. S., Hooper, A., Chen, X., Barletta, V. R., and Bordoni, A.: Reduced ice mass loss and three-dimensional viscoelastic deformation in northern Antarctic Peninsula inferred from GPS, Geophys. J. Int., 222, 1013–1022, https://doi.org/10.1093/gji/ggaa229, 2020.

Scheinert, M., Ivins, E. R., Dietrich, R., and Rülke, A.: Vertical Crustal Deformation in Dronning Maud Land, Antarctica: Observation versus Model Prediction, in: Antarctica, edited by: Fütterer, D. K., Damaske, D., Kleinschmidt, G., Miller, H., and Tessensohn, F., Springer, Berlin, Heidelberg, https://doi.org/10.1007/3-540-32934-X_44, 2006.

Scheinert, M., Shen, W., Aster, R. C., Caron, L., Hartinger, M. D., King, M. A., Lloyd, A., Reading, A. M., Winberry, J. P., Wilson, T., Alfonsi, L., Bentley, M. J., Buchta, E., Chen, T. Y., Clarke, P. J., Ebbing, J., Eisen, O., Gomez, N., Günaydın, E., Hansen, S., Ivins, E. R., Koulali, A., Nield, G. A., Richards, F., Selbesoglu, M. O., Sherman, S., Whitehouse, P. L., and Willen, M.: Geophysics in Antarctica: Achievements, Current Capabilities, and Future Directions, EGUsphere [preprint], https://doi.org/10.5194/egusphere-2025-6370, 2026.

Seroussi, H., Pelle, T., Lipscomb, W. H., Abe-Ouchi, A., Albrecht, T., Alvarez-Solas, J., Asay-Davis, X., Barre, J.-B., Berends, C. J., Bernales, J., Blasco, J., Caillet, J., Chandler, D. M., Coulon, V., Cullather, R., Dumas, C., Galton-Fenzi, B. K., Garbe, J., Gillet-Chaulet, F., Gladstone, R., Goelzer, H., Golledge, N., Greve, R., Gudmundsson, G. H., Han, H. K., Hillebrand, T. R., Hoffman, M. J., Huybrechts, P., Jourdain, N. C., Klose, A. K., Langebroek, P. M., Leguy, G. R., Lowry, D. P., Mathiot, P., Montoya, M., Morlighem, M., Nowicki, S., Pattyn, F., Payne, A. J., Quiquet, A., Reese, R., Robinson, A., Saraste, L., Simon, E. G., Sun, S., Twarog, J. P., Trusel, L. D., Urruty, B., Van Breedam, J., van de Wal, R. S. W., Wang, Y., Zhao, C., and Zwinger, T.: Evolution of the Antarctic Ice Sheet Over the Next Three Centuries From an ISMIP6 Model Ensemble, Earth's Future, 12, e2024EF004561, https://doi.org/10.1029/2024EF004561, 2024.

Shida, T.: On the Elasticity of the Earth and the Earth's Crust, Memoirs of the College of Science and Engineering, Kyoto Imperial University, 4, 1–286, https://books.google.com/books?id=9Ko_AQAAMAAJ (last access: 3 September 2026), 1912.

Simms, A. R., Ivins, E. R., DeWitt, R., Kouremenos, P., and Simkins, L. M.: Timing of the most recent Neoglacial advance and retreat in the South Shetland Islands, Antarctic Peninsula: insights from raised beaches and Holocene uplift rates, Quaternary Sci. Rev., 47, 41–55, https://doi.org/10.1016/j.quascirev.2012.05.013, 2012.

Spada, G. and Boschi, L.: Using the Post–Widder formula to compute the Earth's viscoelastic Love numbers, Geophys. J. Int., 166, 309–321, https://doi.org/10.1111/j.1365-246X.2006.02995.x, 2006.

Spada, G. and Melini, D.: SELEN^4 (SELEN version 4.0): a Fortran program for solving the gravitationally and topographically self-consistent sea-level equation in glacial isostatic adjustment modeling, Geosci. Model Dev., 12, 5055–5075, https://doi.org/10.5194/gmd-12-5055-2019, 2019.

Spada, G., Antonioli, A., Boschi, L., Boschi, L., Brandi, V., Cianetti, S., Galvani, G., Giunchi, C., Perniola, B., Agostinetti, N. P., Piersanti, A., and Stocchi, P.: Modeling Earth's post-glacial rebound, Eos T. Am. Geophys. Un., 85, 62–64, https://doi.org/10.1029/2004EO060007, 2004.

Spada, G., Barletta, V. R., Klemann, V., Riva, R. E. M., Martinec, Z., Gasperini, P., Lund, B., Wolf, D., Vermeersen, L. L. A., and King, M. A.: A benchmark study for glacial isostatic adjustment codes, Geophys. J. Int., 185, 106–132, https://doi.org/10.1111/j.1365-246X.2011.04952.x, 2011.

Swierczek-Jereczek, J., Montoya, M., Latychev, K., Robinson, A., Alvarez-Solas, J., and Mitrovica, J.: FastIsostasy v1.0 – a regional, accelerated 2D glacial isostatic adjustment (GIA) model accounting for the lateral variability of the solid Earth, Geosci. Model Dev., 17, 5263–5290, https://doi.org/10.5194/gmd-17-5263-2024, 2024.

van Calcar, C. J., Whitehouse, P. L., van de Wal, R. S. W., and van der Wal, W.: Approximating 3D bedrock deformation in an Antarctic ice-sheet model for projections, The Cryosphere, 20, 757–775, https://doi.org/10.5194/tc-20-757-2026, 2026.

Wan, J. X. W., Gomez, N., Latychev, K., and Han, H. K.: Resolving glacial isostatic adjustment (GIA) in response to modern and future ice loss at marine grounding lines in West Antarctica, The Cryosphere, 16, 2203–2223, https://doi.org/10.5194/tc-16-2203-2022, 2022.

Weerdesteijn, M. F. M. and Conrad, C. P.: Recent ice melt above a mantle plume track is accelerating the uplift of Southeast Greenland, Communications Earth & Environment, 5, 791, https://doi.org/10.1038/s43247-024-01968-6, 2024.

Whitehouse, P., Bentley, M. J., Milne, G. A., King, M. A., and Thomas, I. D.: A new glacial isostatic adjustment model for Antarctica: calibrated and tested using observations of relative sea-level change and present-day uplift rates, Geophys. J. Int., 190, 1464–1482, 2012.

Whitehouse, P. L.: Glacial isostatic adjustment modelling: historical perspectives, recent advances, and future directions, Earth Surf. Dynam., 6, 401–429, https://doi.org/10.5194/esurf-6-401-2018, 2018.

Wiens, D. A., Shen, W., and Lloyd, A. J.: The seismic structure of the Antarctic upper mantle, Geological Society, London, Memoirs, 56, 195–212, https://doi.org/10.1144/M56-2020-18, 2023.

Wolstencroft, M., King, M. A., Whitehouse, P. L., Bentley, M. J., Nield, G. A., King, E. C., McMillan, M., Shepherd, A., Barletta, V. R., Bordoni, A., Riva, R. E. M., Didova, O., and Gunter, B. C.: Uplift rates from a new high-density GPS network in Palmer Land indicate significant late Holocene ice loss in the southwestern Weddell Sea, Geophys. J. Int., 203, 737–754, https://doi.org/10.1093/gji/ggv327, 2015.

Zhao, C., King, M. A., Watson, C. S., Barletta, V. R., Bordoni, A., Dell, M., and Whitehouse, P. L.: Rapid ice unloading in the Fleming Glacier region, southern Antarctic Peninsula, and its effect on bedrock uplift rates, Earth Planet. Sc. Lett., 473, 164–176, https://doi.org/10.1016/j.epsl.2017.06.002, 2017.